This is to certify that the

dissertation entitled

TRUCK TIRE/PAVEMENT INTERACTION ANALYSIS BY THE FINITE ELEMENT METHOD

presented by

Lan Meng

has been accepted towards fulfillment
of the requirements for

Ph.D. degree in Engineering Mechanics

Major professor

Date 7 December 2001

TRUCK TIRE/PAVEMENT INTERACTION ANALYSIS BY THE FINITE ELEMENT METHOD

By

Lan Meng

DISSERTATION

Submitted to
Michigan State University
in partial fulfillment of the requirements
for the degree of

DOCTOR OF PHILOSOPHY

Department of Materials Science and Mechanics

2002

ABSTRACT

TRUCK TIRE/PAVEMENT INTERACTION ANALYSIS BY THE FINITE ELEMENT METHOD

By

Lan Meng

A simulation is developed for study of interactions between a rolling truck tire and a rigid pavement structure. A three-dimensional finite element method is required to solve this nonlinear dynamic contact problem. The ABAQUS finite element code is employed. A Goodyear 295/75R22.5 Unisteel G167A Low Profile Radial smooth tire is modeled to roll over the rigid pavement. Fiber reinforced composite model and rubber material model is utilized to simulate the real tire structure. The Coulomb friction law is used to study the contact between the truck tire and pavements. Different tire pressure levels, load levels, moving speeds, slip angles, braking or traction, and friction are applied in the simulation. Results for a static loaded tire against a rigid flat plate are compared with experimental data from the literature. Contact stress distributions and contact areas for the rolling tire over the rigid pavement at various conditions are presented.

Results from this investigation lead to the following observations and conclusions:

1. For a free rolling tire model, normal stress contours of the free rolling tire model are shifted forward; high stress areas are moved toward to two sidewalls; high stress areas

are increased in fore-back direction; normal maximum stresses at higher tire pressure (100 psi and 110 psi) are higher than for the static loaded tire.

2. For a free rolling tire model at a deflection of 50 mm and a speed of 65 mph, the ratio between the maximum stress and the average static average is above 2.0 at 100 psi and 110 psi.
3. For traction or braking tire models, normal stress contours for the traction models are shifted forward more than for the free rolling model; normal stress contours for the braking models are shifted backward.
4. For traction or braking tire models, contact areas are larger and contact stress are higher than for the free rolling model.
5. For the slip-rolling tire model, high stress areas are moved toward the sidewalls in the slip direction. The contact areas are smaller than for the free rolling model. The maximum normal stresses are higher than for free rolling models and traction or braking models.
6. For the slip-rolling tire model, a larger slip angle produces higher normal stress and shear stress.
7. The maximum ratios of max/av. stress vary from 1.98 for static case to 1.97 for the free rolling case, and 3.22 for the traction case to 3.29 for the slip rolling case. These findings suggest that the average stress used in the AASHTO seriously underestimates the maximum stresses served by pavements, with the result that highways can be seriously underdesigned.

To My Family

ACKNOWLEDGMENTS

Many people have been very helpful to me throughout my graduate studies. I specially appreciate my advisor Gary Lee Cloud for his encouragement, guidance, and support throughout my study at the Michigan State University.

Thank you to my Ph.D. committee members, Ronald C. Averill, Larry Segerlind, and Zhengfang Zhou for their advice, comment, and help during this project.

Thank you also to Bill Kenis at the Federal Highway Administration for his support and interest and for providing the opportunity for me to do this project.

I thank the Goodyear Company for providing the truck tire information.

Thank you to the Federal Highway Administration for granting me the Dwight David Eisenhower Transportation Fellowship, Michigan State University for granting me the Graduate School Summer Acceleration Fellowship, Cybernet Systems Corp., the Composite Materials and Structure Center (MSU), and the Materials Science and Mechanics Department (MSU) for their financial support.

Last, but not the least, a special thanks go to my husband, Binshan Ye, and my daughter, Mengyuan Ye, for their love, support, and understanding.

TABLE OF CONTENTS

LIST OF TABLES

LIST OF FIGURES

Chapter 1

INTRODUCTION

1.1 Introduction

The effect of traffic loads on pavement performance is a fundamental concern in highway engineering, and it represents one of the most visible aspects of road transportation to the motoring public. Truck performance has become a critical element of highway safety in recent years for two reasons. First, the percentage of trucks in the highway traffic stream has increased dramatically, up to 30 percent on some roadways, according to the American Association of State Highway and Transportation Officials (AASHTO, 1993). Second, trucks are now equipped with very powerful engines that allow them to carry larger loads at higher speeds. The increase in speed and gross weight produces heavy loads on roadways, thus, high quality performance of pavement has become an important requirement.

The safety and efficiency of a truck depend heavily upon the few square inches of tire that are in contact with the ground. This contact area, not much larger than a 3-by-5 inch postcard, is responsible for the load transfer between the truck and the ground during any maneuvering behavior (accelerating, cornering, braking, and so on), on any kind of surface (asphalt, concrete, and so on) in any kind of weather (dry, wet, icy, and so on).

The contact load acts repeatedly and produces damage to the pavement, which eventually leads to the deterioration of the pavement. Clearly, roadbuilders need more accurate data on truck-pavement interaction because it is crucial in determining the impact of trucks on highway safety. This process is very complicated because it involves many analytical aspects that include three mechanical parts. First, pavement is a composite material with several layers. Material properties of each layer can be complex, for they might be elastic, plastic, visco-elastic, visco-plastic, bi-modular, anisotropic and so on. Second, when a load is applied to the pavement, the complexity increases. Vehicles with various suspension and tire structures pass over highways at different speeds or duration of staying on its surface. Vehicle loadings are randomly repeated on pavements. Third, pavement and vehicles impose forces on each other. These applied loads deform the pavement, especially at the surface; this leads to excitation of axle suspensions resulting in ever-greater dynamic load on the pavement structure. The process involves acceleration which causes variations in pavement conditions and vehicle load to reinforce each other through time, and to become more significant as the pavement deteriorates further.

Most of the widely used pavement design methods are based on the principle of "equivalent loads" which involves a traffic axle-load spectrum represented by a static single equivalent design load for the pavement. The equivalent loadings are predicted using the AASHTO method of equivalency factors that was derived from the American Association of State Highway and Transportation Officials Road Test. The test, performed in the late 1950's and early 1960's, may not accurately quantify the effects of many vehicle loading parameters, according to recent studies. Vehicle characteristics such

as tire pressure, suspension types, axle configurations, axle loads and gross vehicle weights have changed significantly since the AASHTO Road Test. This may have the general effect of causing more damage to the pavement than the axle loads and overloads used in the AASHTO Road Test. The equivalency factors developed from the road test tend to underestimate the amount of damage caused to the pavement by modern vehicles.

The most serious limitation of this approach is that it provides no understanding of the actual mechanisms of dynamic interaction between tire load and pavement structure. This lack of insight makes it difficult to adapt the AASHTO concepts to change vehicle or pavement technology. In pavement design, AASHTO uses a static load rather than dynamic load, and uniform tire contact stress distribution is used to simulate tire/pavement contact vertical stresses as input towards the design and evaluation of pavements.

Recently some researchers have started analyzing pavement response under a moving load. In these analyses, a point load or a uniform stress is used for investigating the pavement response. Researchers in both the automotive industry and the highway system are also analyzing tire/pavement contact. But too little data are available for a tire rolling over pavement, so an actual interface stress distribution when a vehicle passes over pavement can not be provided.

The purpose of this study is to investigate the contact stresses caused by a real truck tire rolling over pavement and to better understand the actual interaction between the tire load and the pavement structure. The results will provide data on real contact stresses at the tire/pavement interface. These data should be useful for designing longer lasting, safer pavement.

Chapter 2

BACKGROUND

2.1 Dynamic Analysis of Pavement-tire interaction

For investigating dynamic effects of vehicles on pavements, the two major methods are numerical analysis and experimental analysis. The problem is so complicated that classical theoretical analyses are not efficient.

White, Zaghloul, Anderson, and Smith (1995) analyzed the pavement response under a moving aircraft load by using a three-dimensional finite element model. They modeled pavement as a layered structure with three groups of materials: asphalt mixture, granular material and cohesive soils. The asphalt mixture was modeled as a visco-elastic material, and the granular and fine-grained layers were modeled as elastic-plastic materials. The simulation consisted of a single-wheel load moving repetitively back and forth over the pavement model at a speed of 6.7 kph (4 mph). They approximated the load contact area in the analysis by using a rectangular area and applying average stress on the contact area.

Chatti (1992) developed a dynamic model for analyzing rigid discontinuous pavements subjected to moving transient loads in the time domain and in the frequency domain. He modeled the pavement slabs using a four-noded, twelve-degrees-of-freedom, medium thick-plate bending element. Load transfer mechanisms used a one-dimensional

bar element or a vertical spring element, respectively. The foundation support was represented by either a damped Winkler model (which consists of vertical independent springs) with uniformly distributed frequency-dependent springs and dashpots, or a system of semi-infinite horizontal layers resting on a rigid base or a semi-infinite halfspace. In this analysis the moving load was represented by using a direct shape function method in which the uniformly distributed global moving load vector was composed of zero entries except at the nodes of the elements where the distributed loads are positioned.

Hendrick, Marlow, and Brademeyer (1992) developed methodology to investigate the interaction between vehicle and pavements that involved two parallel components. One component employed computer simulations of various vehicle loads, plus modeling axle configuration, suspension type and behavior, and tire structure and flexing, to predict dynamic loads along the length of the pavement over time. The second component adapted computer simulations of asphalt pavements and portland cement concrete pavements to predict the response of these pavements to moving dynamic loads and to estimate the accumulation of different manifestations of damage over time. Furthermore, the surface profile of the simulated pavement at specified times was used as input to the vehicle model to predict dynamic loads, which in turn were used as inputs to the pavement model to predict subsequent response and deterioration. In the vehicle model simulation, the first mathematical models for each component were developed, then these sub-systems were put together in a simulation program. Rolling was neglected, but vertical motion and pitch were included. The developed models were fully nonlinear, time domain models. In the pavement simulation part, both mathematical and finite

element models were established for flexible and rigid pavement. These parametric studies show that consideration of dynamic loading is necessary and that considerable variation of dynamic loads is produced by alternative tandem axle configurations.

Researchers have developed another major analysis method to evaluate primary response of pavement under traffic loads. In 1990 the Federal Highway Administration (FHWA) constructed a test section on the access road to the Turner Fairbank Research Facility in McLean, VA. They used instrumented pavement test sections in conjunction with instrumented vehicles to measure primary pavement response to the dynamic wheel loads. The test sections consisted of thick and thin sections of asphalt concrete, 178 mm and 89 mm, respectively. Each test section was 30.4m long, separated by a 7.6m transition zone. The road was equipped with longitudinal strain gages and deflectometers. The FHWA vehicle was instrumented with LVDT's between the axles and chassis to measure chassis-axle displacements on both ends of the front and rear axles. The vehicle was also equipped with accelerometers to measure the vertical accelerations, plus strain gages in conjunction with the accelerometers at the ends of each axle to calculate dynamic wheel forces. Tests were conducted at four check speeds including 15 mph, 25 mph, 35 mph, and 45 mph. Three vehicle loads, empty, intermediate, and full were used. This experimental work provides the primary response of the pavement as well as simultaneous displacements of axles and wheel forces under different loads and speeds.

2.2 Tire Contact Patch Analysis

Stress, not force, damages pavement. The contact patch (footprint) is a critical factor in pavement design and analysis. Though engineers have researched contact patches for many years, they are still important problems for highway engineering and the automotive industry. Due to complicated tire structure and geometry, the problem is inherently nonlinear. The most general deformation of a pneumatic tire is in reality a coupled-mechanical-thermodynamic process. Because the material properties of tires are nonhomogenous and anisotropic, composite material theory needs to be applied. In addition to these concerns, both the contact area and the contact load intensities are not known in advance, and they vary during the loading history.

For a moving truck, especially one moving on a highway with a very high speed, getting a footprint is very difficult and expensive. Much experimental analysis has been done in laboratories. Pottinger (1992) discussed the three-dimensional contact patch stress field of solid and pneumatic tires. He based his discussion on experimental studies of a smooth-treaded urethane solid tire and a low-pull-force smooth-treaded radial, to represent solid and pneumatic tires. The results were in static and free rolling states of both tire types. All experiments were performed on the BFGoodrich Flat Surface Tire Dynamic Machine. He discussed footprint size and shape, normal stress, lateral stress and longitudinal stress for solid and pneumatic tires.

de (1994) discussed an experimental vehicle-road surface pressure transducer array (vrspta) system. He designed this system to simultaneously measure vertical, longitudinal, and lateral loads; and load distributions transferred to the road surface by a passing wheel. He based his research on the concept of instrumented and calibrated pins buried in the

surface of the pavement designed to measure loads and load distributions over the complete tire contact area. Strain-gauged load cell pins were installed in a row, at right angles to the direction of travel of the passing wheel. He used a heavy vehicle simulator for different wheel load ranges, different wheel velocities, and one tire pressure in the test. He gathered data on vertical stress distribution, transverse stress distribution and longitudinal stress distributions at the given speeds, loads and tire pressures. The wheel speeds were very low: 4 km/h, 6k m/h and 8 km/h.

The development of nonlinear finite element techniques has enabled researchers to develop comprehensive mathematical tire models. Roberts, Tielking, Middleton, Lytton, and Tseng (1985) developed a finite element model of a free-rolling tire for analyzing the effect of tire inflation pressure and load on pavement contact stresses. In this model an assembly of axisymmetric shell elements was positioned along the carcass mid-ply surface. They used a 10-ply 10.00-20 truck tire. The ply structure in each finite element was specified separately to define the laminated cord-rubber tire carcass. Specifying the lamination of each element separately allowed tire construction features such as belts, sidewall reinforcements, and bead turn-ups to be included in the tire model. The finite elements were homogeneous orthotropic, with moduli determined by the laminated carcass. The elements were connected at the node points. The tire model was loaded first by specifying the inflation pressure. They obtained an axisymmetric solution for the inflated shape. Prior to applying the axle load they calculated structural stiffness of the inflated tire. They brought the model into contact with the pavement by specifying the axle height, which was equivalent to specifying the tire deflection relative to the pavement. The computer tire model was deflected against a frictionless, flat rigid surface.

DeEskinazi, Yang, and Soedel (1978) analyzed a steel belted radial tire in contact with a flat surface by the use of the finite element method. They expressed their cross-sectional profile by two fifth-degree polynomials in x and y. Because of symmetry, only one octant of the tire was modeled. They modeled the tire configuration by using flat triangular plate elements. They divided the radial profile into four zones; each zone was assumed to be homogeneous. Laminate properties were included in the formulation of the stiffness matrix of the triangular plate element. They considered inflation of the tire and vertical loading in the analysis, and they discussed the deflections of the tire and the effect of bending material properties.

Trinko (1984) modeled a steel-belted radial tire subjected to inflation pressure and footprint loading using laminated, geometrically nonlinear finite elements of the MSC/NASTRAN program. He used a one-quarter model to take advantage of symmetry with respect to the meridional plane and a plane perpendicular to the axis of rotation. The analyzed tire had two steel belts and two polyester radial plies. He divided the 180^0 segment into 11 circumferential sections, and smaller subsections were located in and near the eventual footprint. He modeled rubber portions using solid eight-noded hexahedrons and a limited number of six-noded pentahedrons; and he modeled the cord-reinforced layers using four-noded quadrilateral membrane elements. Two belts were described by one layer of membrane plate element.

Ridha, Satyamurthy, Hirschfelt, and Holle (1985a) discussed the contact loading of a rubber disk by using three-dimensional isoparametric elements. They analyzed the contact of a deformable body loaded against rigid surfaces; the body was a 25 mm-thick rubber disk modeled by 12-noded-three-dimensional isoparametric elements. The inflation

pressure and footprint loads were applied on the disk model. In the contact area, both frictionless and no-slip results were discussed. The computed load-deflection responses show good agreement with measured results. The shape and size of the footprint contact were also presented and exhibited good agreement between the computed and measured results. Contact pressures were calculated from the contact force by using the principle of static equivalency of the two force systems. Ridha, Satyamurthy, Hirschfelt, and Holle (1985b) used the same approach to model a homogeneous pneumatic tire subjected to inflation pressures and footprint loads. The computed shapes and sizes of the footprint area at different levels of rim deflection are shown to be in good agreement with experimental results.

Tanner (1996) modeled the Space Shuttle nose-gear tire using a two-dimensional laminated anisotropic shell theory, in which the effects of variation in material and geometric parameters, transverse shear deformation, and geometric nonlinearities were included. In this model he developed a contact algorithm with static friction effects that predict tire response to combined inflation-pressure and static vertical-loading conditions. He also carried out experimental measurements on the Space Shuttle orbiter nose-gear tire to define its response to combined inflation-pressure and static vertical-loading conditions. The predicted normal and tangential contact load intensity distributions were in fair to good agreement with experimental measurements. This author notes that additional experimental and analytical studies are needed.

Faria, et al. (1989, 1992) and Oden, et al. (1988) derived a steady-state formulation for the rolling contact problem with friction. For steady motion the explicit time dependency was removed from the problem. In this analysis the motion of the structure

was decomposed into two successive motions, a point in the structure underwent first a rigid rotation and then moved to the point occupied by the material point at time t. In the contact area, a nonpenetration condition was applied. They used Coulomb friction for stick/slip conditions and a variational formulation for the equilibrium and all boundary conditions. Faria analyzed a viscoelastic spinning cylinder and a passenger tire. In the tire model, the cross section of the tire was represented by a combination of layered anisotropic thick-shell elements in the carcass and belts and isotropic bricks in the tread region. For the contact area (footprint) he used a friction coefficient of 0.51. In Oden's study, a viscoelastic rubber cylinder was analyzed as a numerical example.

Mousseau and Clark (1994) used a ring on an elastic foundation model as a pneumatic tire analog for two-dimensional contact problems. They applied two-node beam elements on the ring model. The problem considered was one of large-deformation, quasi-static contact. The tire was first inflated by incrementally increasing the pressure loading. In this step, the nonlinear solver in the finite element program calculated a series of equilibrium solutions until the specified inflation pressure was reached. While this process took place, position and rotation constraints on the hub prevented the tire from moving. Once inflated, the tire was then pushed onto a flat surface by incrementally decreasing the wheel center height. Finally, the hub rotational constraint was released and the longitudinal position of the ground surface was moved incrementally backward. This motion, along with the friction between the ring elements and ground allowed the tire to roll over surface. They completed these steps by using the ABAQUS nonlinear finite element program. Experimental hub force measurements verified the simulation results, and the experimental results agree with the simulation.

2.3 Research Objectives

Much work has been done in tire/pavement interaction analysis, but very little data are available for a real tire structure rolling over pavement. In this study, actual tire/pavement contact stresses for steady-state moving conditions are analyzed. To complete this task, the finite element method was used to model a real truck tire rolling over a rigid pavement. A three-dimensional tire model with real tire pressure simulated the interaction between a truck tire and a rigid pavement. Different steady-state moving conditions of trucks, tire pressure levels, different tire load levels, and different friction models are considered. The purpose of this work is to find out the effects of these factors on truck tire/pavements interaction. These analyses provide fundamental data and establish mechanisms for understanding truck tire/pavement interaction.

Given the complexity of truck tire/pavement interaction analysis, the average static normal stress of vehicle loads is still used in pavement design. The results of this analysis provide contact information for a steady-state rolling truck tire. The accuracy of the method for considering vehicle loads in pavement design can be evaluated, and improvements to the design procedure can be implemented.

Chapter 3

APPLICATION OF THE FINITE ELEMENT ANALYSIS

3.1 Introduction of ABAQUS/Standard code

Based on the characteristics of truck-pavement interaction, the ABAQUS/Standard finite element code (Hibbitt, Karlsson & Sorensenm Inc. 1998) is chosen for this analysis. ABAQUS is a general-purpose finite element program.

ABAQUS/Standard provides a specialized analysis capability to model the steady-state behavior of a cylindrical deformable body rolling along a flat rigid surface. The capability uses a reference frame that removes the explicit time dependence from the problem so that a purely spatially dependent analysis can be performed. For an axisymmetric body traveling at a constant ground velocity and constant angular rolling velocity, a steady state is possible in a frame that moves at the speed of the ground velocity but does not spin with the body in the rolling motion. This choice of reference frame allows the finite element mesh to remain stationary so that only the part of the body in the contact zone requires fine meshing.

The kinematics of the rolling problem is described in terms of a coordinate frame that moves along with the ground motion of the body. In this moving frame the rigid body rotation is described in a spatial or Eulerian manner and the deformation in a material or

Lagrangian manner. It is this kinematic description that converts the steady moving contact field problem into a purely spatially dependent simulation.

In the following sections of Chapter 3, a brief review of ABAQUS/Standard theories related to this analysis is presented. The information is extracted from the ABAQUS/Standard manual (Hibbitt, Karlsson & Sorensenm Inc. 1998.)

3.2 Governing Equations

Let V denote a volume occupied by a part of the body in the current configuration, and let S be the surface bounding this volume. Let the surface traction at any point be **t** (force per unit of current area), and let the body force at any point within the volume of material under consideration be **f** (per unit of current volume.) Force equilibrium for the volume is then

$$\int_S \mathbf{t} dS + \int_V \mathbf{f} dV = 0 \tag{3-1}$$

The Cauchy stress matrix $\boldsymbol{\sigma}$ at a point of S is defined by

$$\mathbf{t} = \mathbf{n} \cdot \boldsymbol{\sigma} \tag{3-2}$$

where **n** is the unit outward normal to S at the point. Using this definition, the equation of (3-1) becomes

$$\int_S \mathbf{n} \cdot \boldsymbol{\sigma} dS + \int_V \mathbf{f} dV = 0 \tag{3-3}$$

Applying the Gauss theorem to the surface integral in the equilibrium equation gives

$$\int_S \mathbf{n}\cdot\boldsymbol{\sigma}dS = \int_V (\frac{\partial}{\partial \mathbf{x}})\cdot\boldsymbol{\sigma}\mathbf{d}\mathrm{V} \tag{3-4}$$

Since the volume is arbitrary, this equation must apply pointwise in the body, thus providing the differential equation of translational equilibrium:

$$\frac{\partial}{\partial \mathbf{x}}\cdot\boldsymbol{\sigma} + \mathbf{f} = 0 \tag{3-5}$$

Here the test function can be imagined to be a "virtual" velocity field, $\delta\mathbf{v}$, which is completely arbitrary except that it must obey any prescribed kinematic constraints and have sufficient continuity. The "virtual" work rate is

$$\int_V [\frac{\partial}{\partial \mathbf{x}}\cdot\boldsymbol{\sigma} + \mathbf{f}]\cdot\delta\mathbf{v}\mathrm{dV} = 0 \tag{3-6}$$

$$\int_V [\frac{\partial}{\partial \mathbf{x}}\cdot\boldsymbol{\sigma}]\cdot\delta\mathbf{v}\mathrm{dV} = \int_V [(\frac{\partial}{\partial \mathbf{x}})\cdot(\boldsymbol{\sigma}\cdot\delta\mathbf{v}) - \boldsymbol{\sigma} : (\frac{\partial\delta\mathbf{v}}{\partial \mathbf{x}})]\mathrm{dV} \tag{3-7}$$

$$\int_V [\frac{\partial}{\partial \mathbf{x}}\cdot\boldsymbol{\sigma}]\cdot\delta\mathbf{v}dV = \int_S \mathbf{n}\cdot\boldsymbol{\sigma}\cdot\delta\mathbf{v}dS - \int_V \boldsymbol{\sigma} : (\frac{\partial\delta\mathbf{v}}{\partial \mathbf{x}})dV = \int_S \mathbf{t}\cdot\delta\mathbf{v}dS - \int_V \boldsymbol{\sigma} : (\frac{\partial\delta\mathbf{v}}{\partial \mathbf{x}})dV \tag{3-8}$$

Thus, the virtual work statement can be written

$$\int_S \mathbf{t}\cdot\delta\mathbf{v}\mathrm{dS} + \int_V \mathbf{f}\cdot\delta\mathbf{v}\mathrm{dS} = \int_V \boldsymbol{\sigma} : (\frac{\partial\delta\mathbf{v}}{\partial \mathbf{x}})\mathrm{dV} \tag{3-9}$$

The virtual velocity gradient in the current configuration is defined as:

$$\frac{\partial\delta\mathbf{v}}{\partial \mathbf{x}} = \delta\mathbf{L} \tag{3-10}$$

The gradient can be decomposed in to a symmetric and an antisymmetric part:

$$\delta \mathbf{L} = \delta \mathbf{D} + \delta \boldsymbol{\Omega} \tag{3-11}$$

where

$$\begin{aligned} \delta \mathbf{D} &= \mathrm{sym}(\delta \mathbf{L}) = \frac{1}{2}(\delta \mathbf{L} + \delta \mathbf{L}^{\mathrm{T}}) \\ \delta \boldsymbol{\Omega} &= \mathrm{asym}(\delta \mathbf{L}) = \frac{1}{2}(\delta \mathbf{L} - \delta \mathbf{L}^{\mathrm{T}}) \end{aligned} \tag{3-12}$$

Since $\boldsymbol{\sigma}$ is symmetric,

$$\boldsymbol{\sigma} : \delta \boldsymbol{\Omega} = 0 \tag{3-13}$$

The virtual work equation in the classical form is obtained as following:

$$\int_V \boldsymbol{\sigma} : \delta \mathbf{D} dV = \int_S \delta \mathbf{v} \cdot \mathbf{t} dS + \int_V \delta \mathbf{v} \cdot \mathbf{f} dV \tag{3-14}$$

where

$$\delta \mathbf{D} = \frac{1}{2}\left(\frac{\partial \delta \mathbf{v}}{\partial \mathbf{x}} + \left[\frac{\partial \delta \mathbf{v}}{\partial \mathbf{x}}\right]^{\mathrm{T}}\right)$$

In the equilibrium and virtual work equation, the internal virtual work rate term is replaced with the integral over the reference volume of the virtual work rate per reference volume, the equation is written as following:

$$\int_{V^0} \boldsymbol{\tau}^c : \delta \varepsilon dV^0 = \int_S \mathbf{t}^{\mathrm{T}} \cdot \delta \mathbf{v} dS + \int_V \mathbf{f}^{\mathrm{T}} \cdot \delta \mathbf{v} dV \tag{3-15}$$

where dV^0 is the natural reference volume, $\boldsymbol{\tau}^c$ and $\boldsymbol{\varepsilon}$ are any conjugate pairing of material stress and strain measures, and the superscript T means transpose.

The finite element interpolator can be written in general as

$$\mathbf{u} = \mathbf{N}_N \delta v^N \tag{3-16}$$

where $\mathbf{N}_N$ are interpolation functions that depend on some material coordinate system. U^N are nodal variables.

The virtual field, $\delta\mathbf{v}$, must be compatible with all kinematic constrains.

$$\delta\mathbf{v} = \mathbf{N}_N \delta v^N \tag{3-17}$$

Now $\delta\varepsilon$ is the virtual rate of material strain associated with $\delta\mathbf{v}$. Hence, the interpolation assumption gives

$$\delta\boldsymbol{\varepsilon} = \boldsymbol{\beta}_N \delta\mathbf{v}^N \tag{3-18}$$

where β_N is a matrix. It can be written as $\beta_N=\beta_N(\mathbf{x}, \mathbf{N}_N)$. The equilibrium equation is approximated as

$$\delta\mathbf{v}^N \int_{V^0} \boldsymbol{\beta}_N : \boldsymbol{\tau}^c dV^0 = \delta\mathbf{v}^N [\int_S \mathbf{N}_N^T \cdot \mathbf{t} dS + \int_V \mathbf{N}_N^T \cdot \mathbf{f} dV] \tag{3-19}$$

since the $\delta\mathbf{v}^N$ are independent variables, a system of nonlinear equilibrium equations can be written as:

$$\int_{V^0} \boldsymbol{\beta}_N : \boldsymbol{\tau}^c dV^0 = \int_S \mathbf{N}_N^T \cdot \mathbf{t} dS + \int_V \mathbf{N}_N^T \cdot \mathbf{f} dV \tag{3-20}$$

By taking the variation of the equilibrium, equations can be written:

$$\int_{V^0} (d\boldsymbol{\tau}^c : \delta\varepsilon + \boldsymbol{\tau}^c : d\delta\varepsilon) dV^0 - \int_S d\mathbf{t}^T \delta\mathbf{v} dS - \int_S \mathbf{t}^T \delta\mathbf{v} dA^r \frac{1}{A^r} dS - \int_V d\mathbf{f}^T \delta\mathbf{v} dV - \int_V \mathbf{f}^T \delta\mathbf{v} J \frac{1}{J} dS \tag{3-21}$$

Here $J = |dV/dV^0|$, the volume change between the reference and the current volume occupied by a piece of the structure; $A_r = |dS/dS^0|$ is the surface area ratio between the reference and the current configuration. Using the constitutive theory,

$$d\boldsymbol{\tau}^c = \mathbf{H} : d\boldsymbol{\varepsilon} + \mathbf{g} \tag{3-22}$$

The complete Jacobian matrix is obtained as following:

$$K_{MN} = \int_{V^0} \boldsymbol{\beta}_M : \mathbf{H} : \boldsymbol{\beta}_N dV^0 + \int_{V^0} \boldsymbol{\tau}^c : \partial_N \boldsymbol{\beta}_M dV^0 - \int_S \mathbf{N}_M^T \cdot \mathbf{Q}_N^S dS - \int_V \mathbf{N}_M^T \cdot \mathbf{Q}_N^S dV \tag{3-23}$$

Here

$$\partial_N = \partial/\partial u^N \tag{3-24}$$

$$\partial_N \varepsilon = \frac{\partial \varepsilon}{\partial u^N} = \boldsymbol{\beta}_N \tag{3-25}$$

$$\partial_N \mathbf{t} + \mathbf{t} \frac{1}{A_r} \partial_N J = \mathbf{Q}_N^S \tag{3-26}$$

$$\partial_N \mathbf{f} + \mathbf{f} \frac{1}{J} \partial_N J = \mathbf{Q}_N^V \tag{3-27}$$

ABAQUS/Standard generally uses Newton's method as a numerical technique for solving the nonlinear equilibrium equations

3.3 Steady –State Transport Analysis

In Figure 3.1 the body is rotating with a constant angular rolling velocity ω around a rigid axle **T** at $\mathbf{X_0}$, which in turn rotates with constant angular velocity Ω around the fixed cornering axis **n** through point $\mathbf{X_c}$. Then the motion of a particle **X** at time t consists of a rigid rolling rotation to position **Y**,

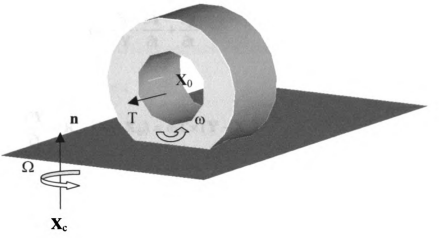

Figure 3.1 Constant cornering motion

$$\mathbf{Y} = \mathbf{R}_s \cdot (\mathbf{X} - \mathbf{X}_0) + \mathbf{X}_0 \tag{3-28}$$

followed by a deformation to point **x**, and a subsequent cornering rotation (or precession) around to position **Y**. So that

$$\mathbf{Y} = \mathbf{R}_s \cdot (\mathbf{x} - \mathbf{X}_c) + \mathbf{X}_c \tag{3-29}$$

where, $\mathbf{R}_s$ is the spinning rotation matrix defined as $\mathbf{R}_s = \exp(\hat{\boldsymbol{\omega}}\mathbf{t})$ and $\hat{\boldsymbol{\omega}}$ is the skew-symmetric matrix associated with the rotation vector $\boldsymbol{\omega} = \omega\mathbf{T}$. The velocity of the particle then becomes

$$\mathbf{v} = \dot{\mathbf{y}} = \dot{\mathbf{R}}_c \cdot (\mathbf{x} - \mathbf{X}_c) + \mathbf{R}_c \cdot \dot{\mathbf{x}} \tag{3-30}$$

where $\mathbf{R}_c$ the cornering rotation given by $\dot{\mathbf{R}}_c = \exp(\hat{\boldsymbol{\Omega}}\mathbf{t})$ and $\hat{\boldsymbol{\Omega}}$ is the skew-symmetric matrix associated with the rotation vector . To describe the deformation of the body, we

define a map $\chi(\mathbf{Y},t)$, which gives the position of point **X** at time t as a function of its location **Y** at time so that $\mathbf{x} = \chi(\mathbf{Y},t)$. It follows that

$$\dot{\mathbf{x}} = \frac{\partial \boldsymbol{\chi}}{\partial \mathrm{Y}} \cdot \frac{\partial \mathbf{Y}}{\partial t} + \frac{\partial \boldsymbol{\chi}}{\partial t} \tag{3-31}$$

where

$$\frac{\partial \mathbf{Y}}{\partial t} = \dot{\mathbf{R}}_s \cdot (\mathbf{X} - \mathbf{X}_0) = \omega \mathbf{T} \times (\mathbf{Y} - \mathbf{X}_0) \tag{3-32}$$

Noting that

$$\dot{\mathbf{R}}_s = \hat{\boldsymbol{\omega}} \cdot \dot{\mathbf{R}}_s = \omega \hat{\mathbf{T}} \cdot \mathbf{R}_s \tag{3-33}$$

and introducing the circumferential direction

$$\mathbf{S} = \mathbf{T} \times (\mathbf{Y} - \mathbf{X}_0)/\mathrm{R} \tag{3-34}$$

where $\mathrm{R} = |\mathbf{Y} - \mathbf{X}_0|$ is the radius of a point on the reference body. So that

$$\dot{\mathbf{x}} = \omega \mathrm{R} \frac{\partial \boldsymbol{\chi}}{\partial \mathbf{Y}} \cdot \mathbf{S} + \frac{\partial \boldsymbol{\chi}}{\partial t} = \omega \mathrm{R} \frac{\partial \boldsymbol{\chi}}{\partial \mathrm{S}} + \frac{\partial \boldsymbol{\chi}}{\partial t} \tag{3-35}$$

where $\mathrm{S} = \mathbf{S} \cdot \mathbf{Y}$ is the distance-measuring coordinate along the streamline. Using this result. Together with

$$\dot{\mathbf{R}}_c = \hat{\boldsymbol{\Omega}} \cdot \dot{\mathbf{R}}_s = \Omega \hat{\mathbf{n}} \cdot \mathbf{R}_s \tag{3-36}$$

the velocity of the particle can be written as

$$\mathbf{v} = \Omega \mathbf{n} \times (\mathbf{y} - \mathbf{X}_c) + \omega \mathbf{R}_c \cdot \frac{\partial \boldsymbol{\chi}}{\partial \mathrm{S}} + \mathbf{R}_c \cdot \frac{\partial \boldsymbol{\chi}}{\partial t} \tag{3-37}$$

The acceleration is obtained by a second differentiation and some manipulation:

$$\mathbf{a} = \Omega^2(\mathbf{nn} - \mathbf{I})\cdot(\mathbf{y} - \mathbf{X}_c) + 2\omega\omega\Omega\mathbf{n}\times\mathbf{R}_c\cdot\frac{\partial\chi}{\partial S} + 2\Omega\mathbf{n}\times\mathbf{R}_c\cdot\frac{\partial\chi}{\partial t} + \omega^2 R^2\mathbf{R}_c\cdot\frac{\partial^2\chi}{\partial S^2} + 2\omega\omega\mathbf{R}_c\cdot\frac{\partial^2\chi}{\partial S\partial t} + \mathbf{R}_c\cdot\frac{\partial^2\chi}{\partial t^2} \tag{3-38}$$

To obtain expression for the velocity and acceleration in the reference frame tired to the body, using the transformations

$$\mathbf{v}_r = \mathbf{R}_c^T\cdot\mathbf{y} \tag{3-39}$$

$$\mathbf{a}_r = \mathbf{R}_c^T\cdot\mathbf{a} \tag{3-40}$$

It is obtained that

$$\mathbf{v}_r = \Omega\mathbf{n}\times(\mathbf{x} - \mathbf{X}_c) + \omega R\frac{\partial\chi}{\partial S} + \mathbf{R}_c\cdot\frac{\partial\chi}{\partial t} \tag{3-41}$$

$$\mathbf{a}_r = \Omega^2(\mathbf{nn} - \mathbf{I})\cdot(\mathbf{x} - \mathbf{X}_c) + 2\omega\Omega R\mathbf{n}\times\frac{\partial\chi}{\partial S} + 2\Omega\mathbf{n}\times\frac{\partial\chi}{\partial t} + \omega^2 R^2\frac{\partial^2\chi}{\partial S^2} + 2\omega R\frac{\partial^2\chi}{\partial S\partial t} + \frac{\partial^2\chi}{\partial t^2} \tag{3-42}$$

For steady-state conditions these expressions reduce to

$$\mathbf{v}_r = \Omega\mathbf{n}\times(\mathbf{x} - \mathbf{X}_c) + \omega R\frac{\partial\chi}{\partial S} \tag{3-43}$$

$$\mathbf{a}_r = \Omega^2(\mathbf{nn} - \mathbf{I})\cdot(\mathbf{x} - \mathbf{X}_c) + 2\omega\Omega R\mathbf{n}\times\frac{\partial\chi}{\partial S} + \omega^2 R^2\frac{\partial^2\chi}{\partial S^2} \tag{3-44}$$

The first term of right hand side of (3-44) can be identified as the acceleration that gives rise to centrifugal forces resulting from rotation about **n**. Noting that $\omega R\frac{\partial\chi}{\partial S}$ is a measure of velocity, the second term can be identified as the acceleration that gives rise to Coriolis forces. The last term combines the acceleration that gives rise to Coriolis and centrifugal forces resulting from rotation about **T**. When the deformation is uniform

along the circumferential direction, this Coriolis effect vanishes so that the acceleration gives rise to centrifugal forces only.

The virtual work contribution from the d'Alembert forces is

$$\delta\Pi = -\int_V \rho \cdot \delta \mathbf{v} dV \tag{3-45}$$

$$\begin{aligned} \delta\Pi = &-\rho\Omega^2 \int_V (\mathbf{x} - \mathbf{X_c}) \cdot (\mathbf{nn} - \mathbf{I}) \cdot \delta \mathbf{v} dV - \\ &2\rho\omega\Omega R \int_V \mathbf{n} \times \frac{\partial \chi}{\partial S} \cdot \delta \mathbf{v} dV + \rho\omega^2 R^2 \int_V \frac{\partial \chi}{\partial S} \cdot \frac{\partial \delta v}{\partial S} dV \end{aligned} \tag{3-46}$$

and the rate of virtual work becomes

$$\begin{aligned} d\delta\Pi = &-\rho\Omega^2 \int_V d\mathbf{x} \cdot (\mathbf{nn} - \mathbf{I}) \cdot \delta \mathbf{v} dV - \\ &2\rho\omega\Omega R \int_V \mathbf{n} \times \frac{\partial d\chi}{\partial S} \cdot \delta \mathbf{v} dV + \rho\omega^2 R^2 \int_V \frac{\partial d\chi}{\partial S} \cdot \frac{\partial \delta v}{\partial S} dV \end{aligned} \tag{3-47}$$

For points on the surface of the deformable body

$$\mathbf{v_D} = \Omega \mathbf{n} \times (\mathbf{x} - \mathbf{X_c}) + \omega R \frac{\partial \chi}{\partial S} + \mathbf{R_c} \cdot \frac{\partial \chi}{\partial t} \tag{3-48}$$

where $\mathbf{n}$ is the cornering axis (which must be normal to the rigid surface) and Ω is the cornering angular velocity around $\mathbf{n}$. Assuming that the velocity of a point on the foundation (or rigid surface) is $\mathbf{v_R}$, the relative motion becomes

$$\mathbf{v_D} - \mathbf{v_R} = \Omega \mathbf{n} \times (\mathbf{x} - \mathbf{X_c}) + \omega R \frac{\partial \chi}{\partial S} + \mathbf{R_c} \cdot \frac{\partial \chi}{\partial t} - \mathbf{v_R} \tag{3-49}$$

where $\mathbf{r} = \mathbf{x} - \mathbf{X_c}$. This equation can be split into normal and tangential components. The rate of penetration is

$$\dot{h} = -\mathbf{n} \cdot \mathbf{v} = -\mathbf{n} \cdot \mathbf{v_R} - \omega R \mathbf{n} \cdot \frac{\partial \chi}{\partial S} - \mathbf{n} \cdot \frac{\partial \chi}{\partial t} \tag{3-50}$$

For any point in contact

$$\mathbf{n} \cdot \frac{\partial \chi}{\partial S} = 0 \tag{3-51}$$

Hence,

$$\dot{h} = -\mathbf{n} \cdot \mathbf{v} = -\mathbf{n} \cdot \mathbf{v}_R - \mathbf{n} \cdot \frac{\partial \chi}{\partial t} \tag{3-52}$$

which in incremental form reduces to the standard contact condition

$$\Delta h = \mathbf{n} \cdot (\Delta \mathbf{x}_R - \Delta \mathbf{x}_D) \tag{3-53}$$

For steady-state conditions

$$\begin{aligned} \mathbf{n} \cdot \Delta \mathbf{x}_R &= 0 \\ \Delta \mathbf{x}_D &= 0 \end{aligned} \tag{3-54}$$

Similarly, the rate of slip is

$$\dot{\gamma} = \mathbf{t}_\alpha \cdot \mathbf{v} = \Omega \mathbf{t}_\alpha \cdot (\mathbf{n} \times \mathbf{r}) + \omega R \mathbf{t}_\alpha \cdot \frac{\partial \chi}{\partial S} - \mathbf{t}_\alpha \cdot \frac{\partial \chi}{\partial t} + \mathbf{t}_\alpha \cdot \mathbf{v}_R \tag{3-55}$$

where $\mathbf{t}_\alpha$ (α=1,2) are two orthogonal unit vector tangent to the contact surface so that $\mathbf{n} = \mathbf{t}_1 \times \mathbf{t}_2$. For steady-state conditions

$$\frac{\partial \chi}{\partial t} = 0 \tag{3-56}$$

So

$$\dot{\gamma} = \mathbf{t}_\alpha \cdot \mathbf{v} = \Omega \mathbf{t}_\alpha \cdot (\mathbf{n} \times \mathbf{r}) + \omega R \mathbf{t}_\alpha \cdot \frac{\partial \chi}{\partial S} + \mathbf{t}_\alpha \cdot \mathbf{v}_R \tag{3-57}$$

Variations in $\dot{\gamma}_R$ yield

$$\delta\dot{\gamma} = \mathbf{t}_\alpha \cdot \mathbf{v} = \Omega \mathbf{t}_\alpha \cdot (\mathbf{n} \times \delta\mathbf{r}) + \omega R \mathbf{t}_\alpha \cdot \frac{\partial \delta\boldsymbol{\chi}}{\partial S} + \mathbf{t}_\alpha \cdot \delta\mathbf{v}_R \tag{3-58}$$

To complete the formulation, a relationship between frictional stress and slip velocity must be developed. A Coulomb friction law is provided for steady-state rolling. The law assumes that slip occurs if the frictional stress,

$$\tau_{eq} = \sqrt{\tau_1^2 + \tau_2^2} \tag{3-59}$$

is equal to the critical stress, $\tau_{crit} = \mu p$, where τ_1 and τ_2 are shear stresses along t_α, μ is the friction coefficient, and p is the contact pressure. On the other hand, when $\tau_{eq} \langle \tau_{crit}$, no relative motion occurs. The condition of no relative motion is approximated in ABAQUS by stiff viscous behavior

$$\tau_\alpha = \kappa_s \dot{\gamma}_\alpha^v \tag{3-60}$$

where $\dot{\gamma}_\alpha^v$ is the tangential slip velocity and κ_s is the "stick viscosity," which follows from the relation

$$\kappa_s = \frac{\tau_{crit}}{\dot{\gamma}_{crit}} \tag{3-61}$$

The allowable viscous slip velocity is defined as a fraction of the circumferential velocity

$$\dot{\gamma}_{crit} = 2F_f \omega R \tag{3-62}$$

where F_f is a user-defined slip tolerance.

These expressions contribute to the standard virtual work contribution for slip,

$$\delta\Pi = \iint_A \tau_\alpha \delta\gamma_\alpha \, dA \tag{3-63}$$

and rate of virtual work for slip,

$$d\delta\Pi = \iint_A (d\tau_\alpha \delta\gamma_\alpha + \tau_\alpha d\delta\gamma_\alpha) dA \qquad (3\text{-}64)$$

3.4 Reinforcing Elements in the Analysis

Reinforcing in elements is defined by using REBAR option. Rebars are defined unaxial reinforcement in solid, membrane, shell, and beam elements. Rebars have material properties that are distinct from those of the underlying element Rebars can be defined as individual reinforcing bars in beam and solid elements. Rebars can also be defined as layers of uniformly spaced reinforcing bars in shell, membrane, and solid elements. Rebars do not contribute to the mass of the model.

Let g_i, i=1, 2, be the element's usual isoparametric coordinates. Let r be an isoparametric coordinate along the line where the face of the element intersects the plane of reinforcement, with $-1 \le r \le 1$ in an element. The plane of reinforcement is always perpendiclar to the element face. The detailed information is shown in Figure 3.2

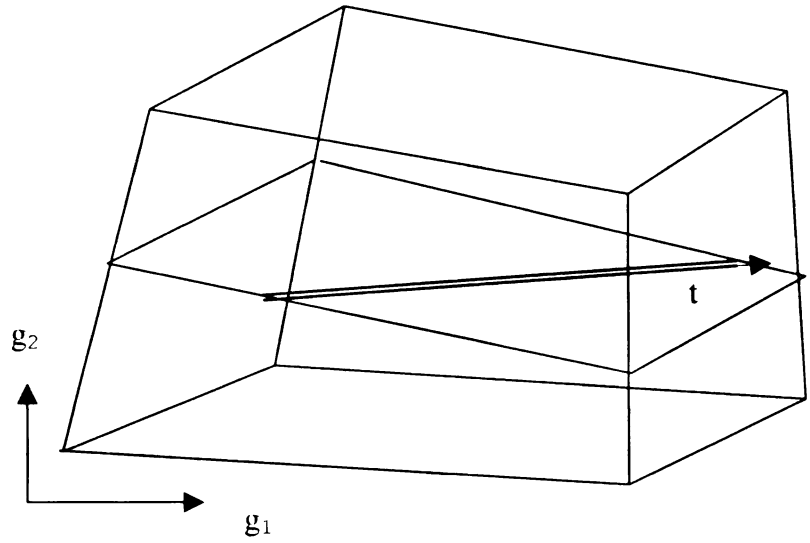

Figure 3.2 Rebar in a solid, two-dimensional element.

The volume of integration(ΔV), and rebar strain (ε) are calculated as

$$\Delta V = \frac{A_r}{S_r}\left(\frac{\partial \mathbf{x}}{\partial r}\cdot\frac{\partial \mathbf{x}}{\partial r}\right)^{\frac{1}{2}} t_0 W_N \tag{3-65}$$

where

$t_0 = 2\pi x_1$

A_0 = rebar cross-sectional area

S_0 = spacing of rebar

W_N = Gauss weight associated with the integration point along the (r) line,

$\mathbf{x} = \mathbf{x}(g_i)$ is position.

$$\frac{\partial \mathbf{x}}{\partial r} = \frac{\partial \mathbf{x}}{\partial g_i}\frac{\partial g_i}{\partial r} \tag{3-66}$$

Strain is

$$\varepsilon = \frac{1}{2}\ln\left(\frac{dl^2}{dl_0^2}\right) \tag{3-67}$$

where dl and dl_0 measure length along the rebar in the current and initial configurations. For the deformation allowed in these elements,

$$\left(\frac{dl^2}{dl_0^2}\right)^2 = \cos^2\alpha\lambda_r^2 + \sin^2\alpha\lambda_t^2 \tag{3-68}$$

where α is the orientation for the rebar from the plane of the model,

$$\lambda_r^2 = \frac{\partial \mathbf{x}}{\partial r}\cdot\frac{\partial \mathbf{x}}{\partial r} \Big/ \frac{\partial \mathbf{x}_0}{\partial r}\cdot\frac{\partial \mathbf{x}_0}{\partial r} \tag{3-69}$$

is the squared stretch ratio in the r-direction, and λ_t ($\lambda_t = x_1 / x_0$ for axisymmetric elements) is the stretch ratio in the t-direction.

3.5 Major Materials Used in the Tire Model

3.5.1 Incompressible Mooney-Rivlin Rubber

It is known that the tread part of a truck tire is made of rubber material. In this analysis the Mooney-Rivlin model is applied on the tread part. The strain energy density function is defined in terms of the input constant A, B and Poission's ratio, ν, as :

$$W(I_1, I_2, I_3) = A(I_1 - 3) + B(I_2 - 3) + C\left(\frac{1}{I_2} - 1\right) + D(I_3 - 1)^2 \tag{3-70}$$

where

$$D = \frac{A(5\nu - 2) + B(11\nu - 5)}{2(1 - 2\nu)} \tag{3-71}$$

$$C = 0.5A + B \tag{3-72}$$

G = 2 (A + B) = shear modulus of linear of elasticity

I_1, I_2, I_3 = strain invariant in terms of the principal stretches

$$I_1 = \lambda_1^2 + \lambda_2^2 + \lambda_3^2 \tag{3-73}$$

$$I_2 = \lambda_1^2 \lambda_2^2 + \lambda_2^2 \lambda_3^2 + \lambda_3^2 \lambda_1^2 \tag{3-74}$$

$$I_3 = \lambda_1^2 \lambda_2^2 \lambda_3^2 \tag{3-75}$$

The principal components of Cauchy stress, σ_i are given

$$J\sigma_i = \lambda_i \frac{\partial w}{\partial \lambda_i} \tag{3-76}$$

The derivation of the constants C and D is completed by considering uniform dilation. For uniform dilation

$$\lambda_1 = \lambda_2 = \lambda_3 = \lambda \tag{3-77}$$

thus the pressure p, is obtained

$$p = \sigma_1 = \sigma_2 = \sigma_3 = \frac{2}{\lambda^3}\left(\lambda^2 \frac{\partial w}{\partial I_1} + 2\lambda^4 \frac{\partial w}{\partial I_2} + \lambda^6 \frac{\partial w}{\partial I_3}\right) \tag{3-78}$$

The relative volume, V can be defined in terms of the stretches as:

$$V = \lambda^3 = \frac{volume_{new}}{volume_{old}} \tag{3-79}$$

For small volumetric deformations, the bulk modulus K, can be defined as the ratio of the pressure over the volumetric strain as the relative volume approaches unity:

$$K = \lim_{V \to 0}\left(\frac{p}{V - 1}\right) \tag{3-80}$$

In the limit, as the stretch approaches 1 the pressure must approach zero. So equation (3-78) must approach zero as the stretch approaches one. With this condition and equation (3-80) the constants C and D can be solved.

3.5.2 Orthotropic Composite Material

The material law that relates stresses to stains is defined as:

$$C = T^T C_L T \tag{3-81}$$

where T is a transformation matrix, and C_L is the constitutive matrix defined in terms of the material constants of the orthogonal material axes, a, b and c. The inverse of C_L is defined as

$$C_L^{-1} = \begin{bmatrix} \frac{1}{E_a} & -\frac{\nu_{ba}}{E_b} & -\frac{\nu_{ca}}{E_c} & 0 & 0 & 0 \\ -\frac{\nu_{ab}}{E_a} & \frac{1}{E_b} & -\frac{\nu_{cb}}{E_c} & 0 & 0 & 0 \\ -\frac{\nu_{ac}}{E_a} & -\frac{\nu_{bc}}{E_b} & \frac{1}{E_c} & 0 & 0 & 0 \\ 0 & 0 & 0 & \frac{1}{G_{ab}} & 0 & 0 \\ 0 & 0 & 0 & 0 & \frac{1}{G_{bc}} & 0 \\ 0 & 0 & 0 & 0 & 0 & \frac{1}{G_{ca}} \end{bmatrix} \tag{3-82}$$

Note that

$$\frac{\nu_{ab}}{E_a} = \frac{\nu_{ba}}{E_b}; \frac{\nu_{ca}}{E_c} = \frac{\nu_{ac}}{E_a}; \frac{\nu_{cb}}{E_c} = \frac{\nu_{bc}}{E_b} \tag{3-83}$$

Chapter 4

SIMULATION OF TIRE/PAVEMENT INTERACTION AND STATIC ANALYSIS

4.1 Description of Tire/Pavement Modeling

In this analysis, a Goodyear 295/75R22.5 Unisteel G167A Low Profile Radial smooth tire is modeled. The design maximum load of the tire is 6175 lbs (27479 N) at 110 psi for a single wheel and 5675 lbs (25254 N) at 100 psi for each wheel of a dual wheel. The tread of the tire has 5 plies of steel cord; the sidewall has 1 ply of steel cord. The overall diameter of the tire is 40.77 inches (inflated); A typical tire structure of this kind of tire is shown in Figure 4.1. The tire information is provided by Smithers Scientific Services, Inc. (Akron, Ohio). The rim data required for this tire is obtained from the Tire and Rim Handbook (1993).

A rigid pavement was considered in this analysis.

4.2 The Finite Element Model

The tire model consists of the following parts: ply, belts, tread cap, sidewall, bead, and flipper. The axisymmetric finite element meshes of the cross-section of the body are used as a starting point. The model is discretized with axisymmetric elements. The cross-section of the tire model is shown in Figure 4.2. The ply and belts are modeled by

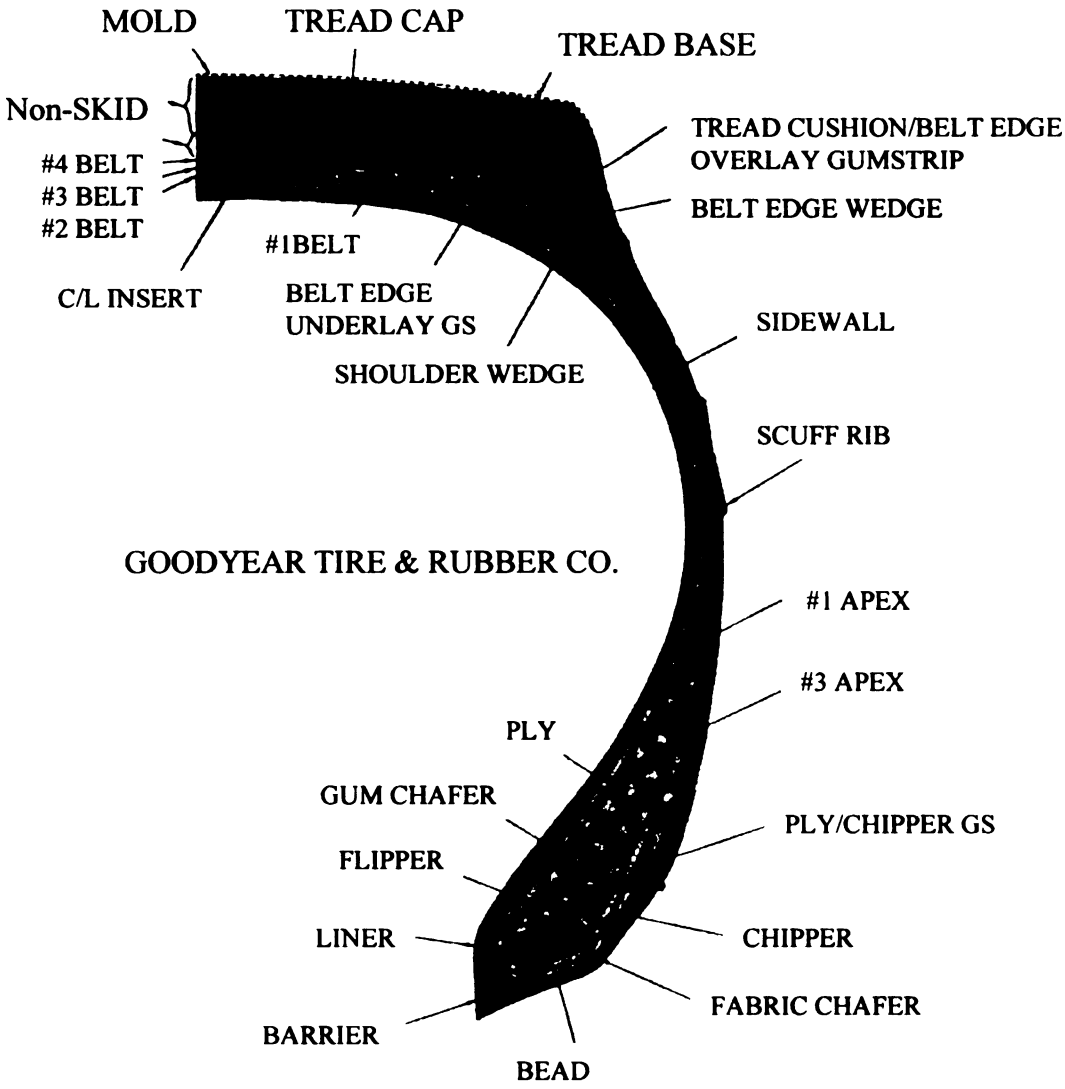

Figure 4.1 Typical tire structure

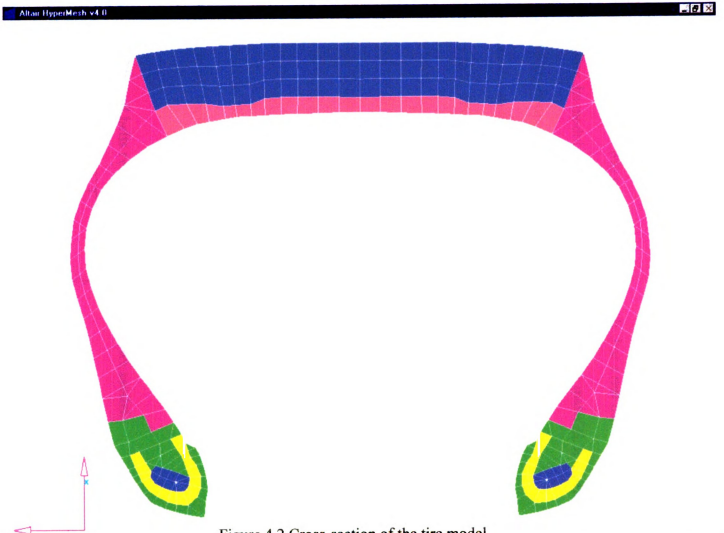

Figure 4.2 Cross-section of the tire model

defining rebar in the continuum elements. They are constructed from fiber reinforced rubber composites. Bead and flipper are modeled as a linear elastic material. The tread and sidewall are made of rubber. The rubber is modeled as an incompressible hyperelastic material, and the fiber reinforcement is model as a linear elastic material. To save computing time, the rim was modeled as a rigid body. For a real truck tire, the rim is made of alloy. Its modulus is much higher than that of rubber material. It is often modeled as a rigid body in tire analysis.

A three-dimensional model is created by revolving the cross-section about the symmetry axis. The axisymmetric elements are converted to three-dimensional continuum elements during the model generation. Fifty divisions make up the circumferential direction of the tire. To refine the mesh in the contact zone, a higher density of elements is chosen in this area. The road is defined as a rigid surface in the three-dimensional model. The truck tire/pavement model, shown in Figure 4.3, has a total of 16600 elements.

The material properties for the tire model were provided by the Goodyear Company (Akron, Ohio). They are listed in the Table 4.1, Table 4.2, and Table 4.3.

Table 4.1 Ply and belts reinforcement properties of tire model.

Part	E, Mpa	□
Bar 1	151580.0	0.3
Bar 2	110240.0	0.3

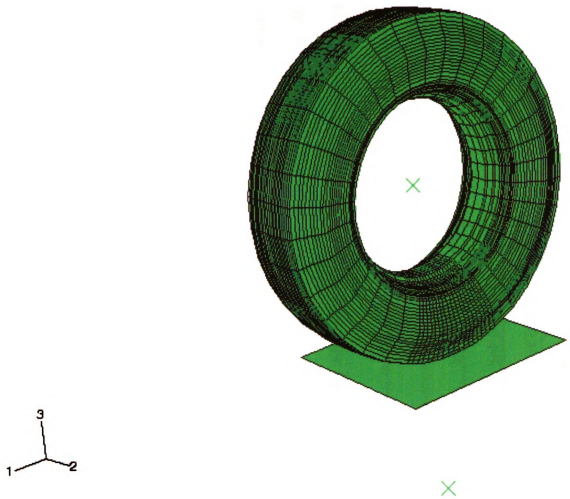

Figure 4.3 Truck tire/pavement model

Table 4.2 Bead and flipper properties of tire model.

Part	E, Mpa	ν
Bead	151580.0	0.3
Flipper	110240.0	0.3

Table 4.3 Rubber properties of tire model.

Part	A, Mpa	B, Mpa	ν
tread	1.1	0.0	0.495
rubber at bead area	5.52	0.0	0.495
Rubber at side wall	3.0	0.0	0.495
Rubber at belts	1.1	0.0	0.495

In this analysis a rotating tire is simulated by three steps: (1) applying tire pressure; (2) applying vertical deflection which is equivalent to load; and (3) rotating the tire with different speeds and accelerations.

For the static part only the first two steps are applied. In the first step, the pressure is applied on the inner surface of the tire model. In this analysis three pressure levels are considered: 90 psi, 100 psi, and 110 psi. In the second step an upward vertical displacement was applied on the rigid pavement to contact with the tire model for a given pressure.

4.3 Validation of the Simulated Tire Model

In this analysis the load-deflection ratio of the tire was used for validating the tire model. The load-deflection curve, widely used for both numerical and experimental analysis, is a very important factor in tire/pavement interaction analysis. The deflection of the tire is defined as the displacement of the tire axis after applying load on it. In static analysis three tire pressure levels are used: 90 psi, 100 psi and 110 psi. Load-deflection curves for three pressure levels are presented in Figure 4.4, Figure 4.5, and Figure 4.6. Experimental results prepared by Goodyear (Akron, Ohio) are presented also. The differences between FEA results and relative experimental results are increased as deflection increased. The differences are 21%, 15.7%, and 16.8% at a deflection of 50.8 mm for pressure of 90 psi, 100 psi, and 110 psi. The mass of the tire is 119.38 lbs. The mass of FEA tire model is 115.79 lbs. Contour maps showing the total deformation at inflation pressure of 100 psi and different deflections are presented in Figure 4.7 to Figure 4.11.

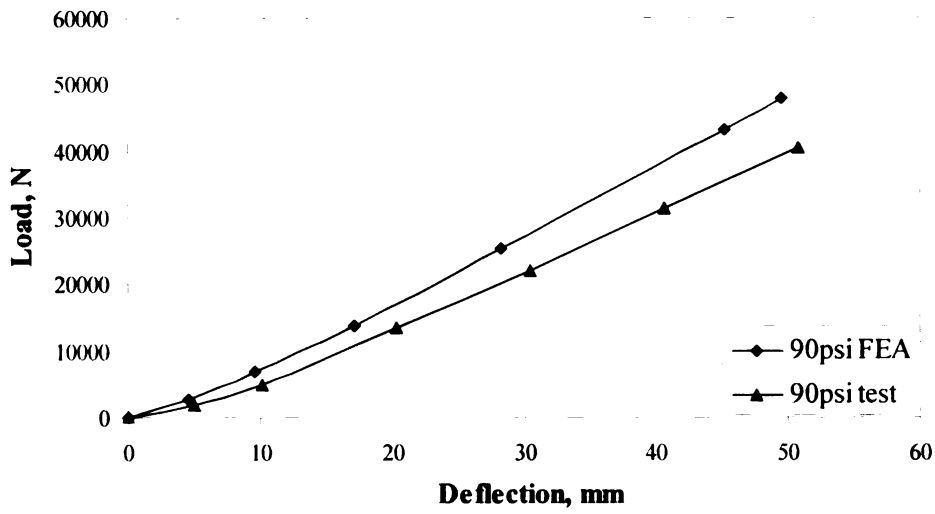

Figure 4.4 Load-deflection curves for the experimental analysis and the numerical analysis (90psi)

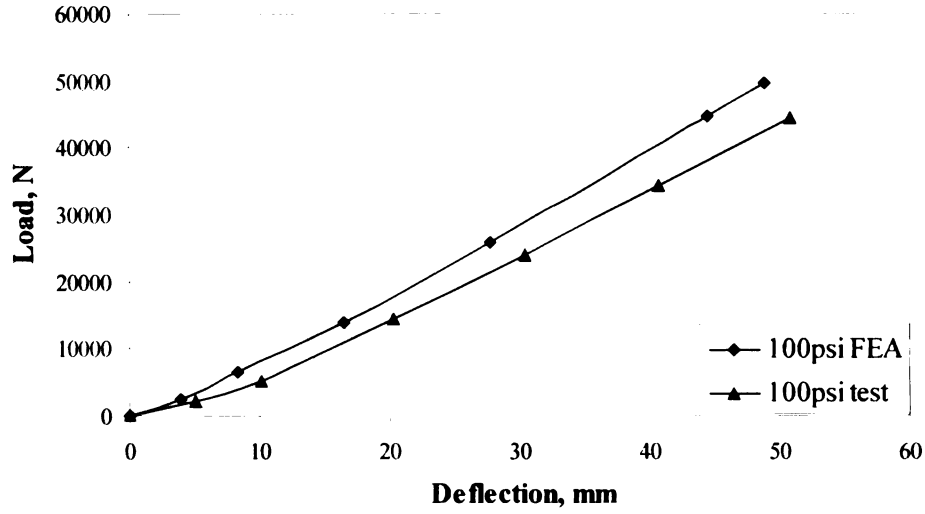

Figure 4.5 Load-deflection curves for the experimental analysis and the numerical analysis (100psi)

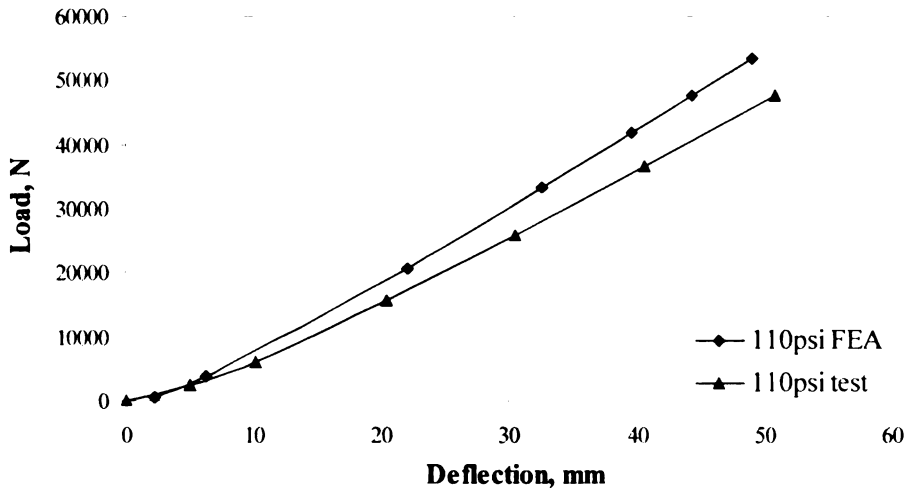

Figure 4.6 Load-deflection curves for the experimental analysis and the numerical analysis (110psi)

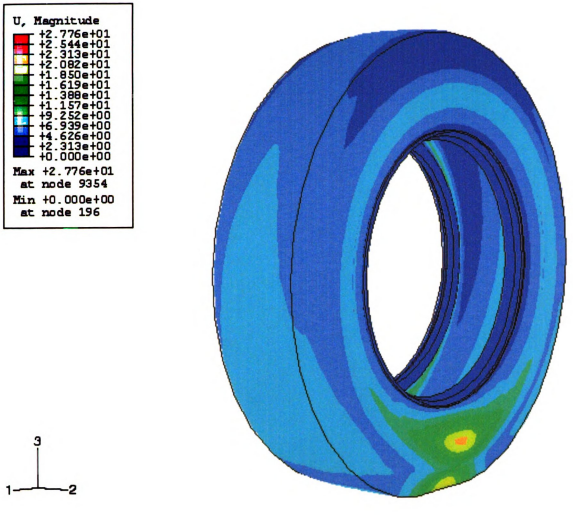

Figure 4.7 Total deformation contours at pressure of 100 psi and deflection of 3.9 mm (2379 N)

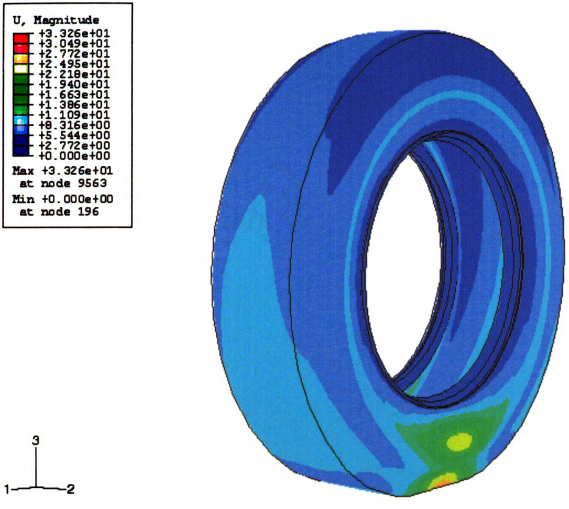

Figure 4.8 Total deformation contours at pressure of 100 psi and deflection of 16.4 mm (13953 N)

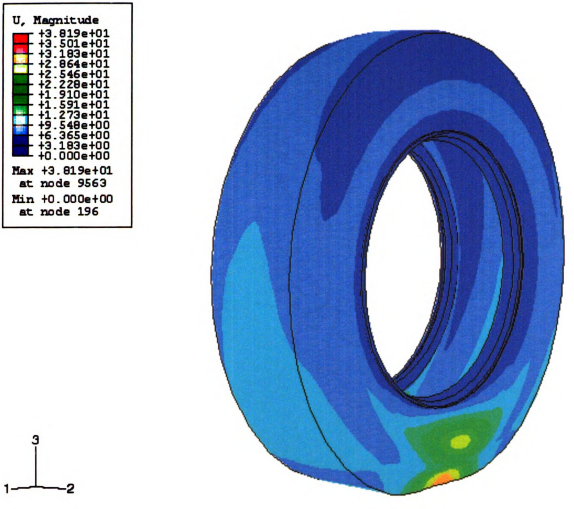

Figure 4.9 Total deformation contours at pressure of 100 psi and deflection of 27.7 mm (25961 N)

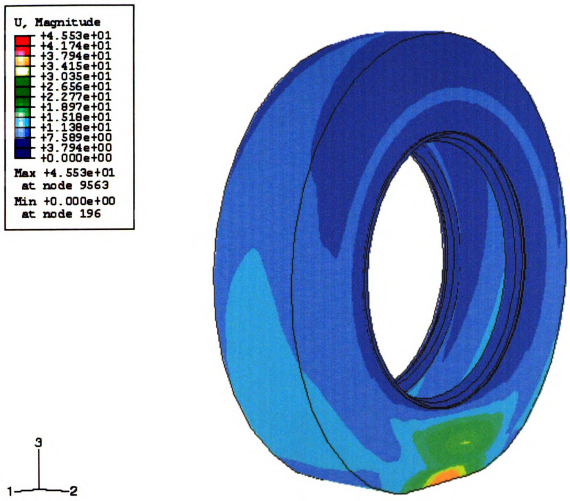

Figure 4.10 Total deformation contours at pressure of 100 psi and deflection of 44.6 mm (44688 N)

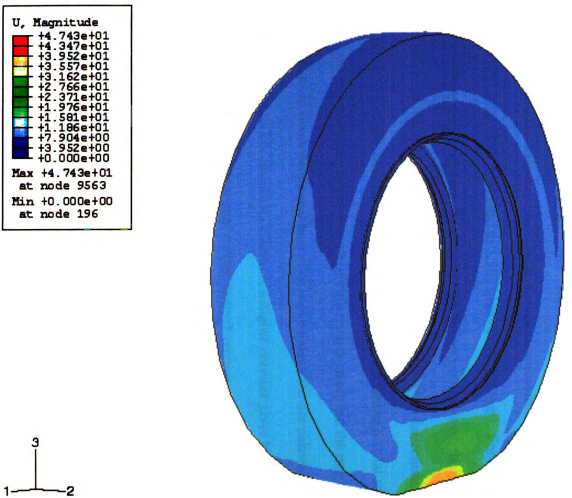

Figure 4.11 Total deformation contours at pressure of 100 psi and deflection of 48.9 mm (49613 N)

4.4 Static Results for the Contact Stress

For the three pressure levels used, summaries of these results are listed in Table 4.4, Table 4.5 and Table 4.6 for pressures of 90psi, 100psi, and 110psi respectively. Representative contact stress distributions are presented in Figures 4.12 to Figure 4.28.

For a pressure of 90psi, the absolute maximum normal stress level varies from 0.343 Mpa (defl=4.6 mm) to 1.433 Mpa (defl=49.6 mm). For a pressure of 100 psi, the absolute maximum normal stress level varies from 0.2938 Mpa (defl=3.9mm) to 1.540 Mpa (defl=48.9 mm). For a pressure of 110 psi, the absolute maximum normal stress level is from 0.0392 Mpa (defl=1.04 mm) to 1.584 Mpa (defl=48.4 mm). For the same pressure level the following results are found: (1) When deflection increases, the maximum stress level increases. (2) Contact shapes and sizes are different when deflections are different; contact areas increase as deflections increase. (3) The maximum normal stress is located at the center part of the contact area when deflection is small, but the maximum normal stress occurs in two separate patches which move toward the tire sidewalls when deflection is large. For the same deflection, a higher pressure gives higher maximum normal stress level. As mentioned earlier, normal average stress is used in pavement design. From Tables 4.4 to 4.6, one sees that some average normal stresses are about half of the corresponding maximum normal stresses. If pressure or deflection is higher, the ratio of Max./Av. is higher. The data show that error is high at high pressure and deflection if the average normal stress is used in pavement design.

Table 4.4 Results of normal stress for tire pressure of 90 psi

Tire deflection, mm	Contact Area, mm^2	Av. stress, Mpa	Max. stress, Mpa	Max./Av.	Figure No.
4.6	8495	0.3271	0.3433	1.0495	Fig. 4-12
9.6	18085	0.3814	0.6128	1.6067	Fig. 4-13
17.6	29200	0.4760	0.8865	1.6824	Fig. 4-14
28.3	40551	0.6240	1.1170	1.7900	Fig. 4-15
45.2	58453	0.7377	1.4330	1.9425	Fig. 4-16
49.6	63482	0.7529	1.4920	1.9817	Fig. 4-17

Table 4.5 Results of normal stress for tire pressure of 100 psi

Tire deflection, mm	Contact Area, mm^2	Av. stress, Mpa	Max. stress, Mpa	Max./Av.	Figure No.
3.9	8321	0.2914	0.2938	1.0082	Fig. 4-18
8.4	17198	0.3913	0.5937	15173	Fig. 4-19
16.4	28477	0.4977	0.8925	1.7932	Fig. 4-20
27.7	39726	0.6649	1.1520	1.7326	Fig. 4-21
45.6	57491	0.7936	1.4710	1.8536	Fig. 4-22
48.9	63686	0.7961	1.540	1.9344	Fig. 4-23

Table 4.6 Results of normal stress for tire pressure of 110 psi

Deflection, mm	Contact Area, mm^2	Av. stress, Mpa	Max. stress, Mpa	Max./Av.	Figure No.
1.04	4886	0.061	0.0392	0.6544	
6.8	14940	0.3321	0.4818	1.4508	Fig. 4-24
14.6	26368	0.4896	0.8516	1.7394	Fig. 4-25
26.3	39701	0.6644	1.1660	1.7550	Fig. 4-26
43.8	57141	0.8352	1.5080	1.8056	Fig. 4-27
48.4	62782	0.8501	1.5840	1.8633	Fig. 4-28

Figure 4.12 Normal stress contour at pressure of 90 psi and deflection of 4.6 mm (2779 N)

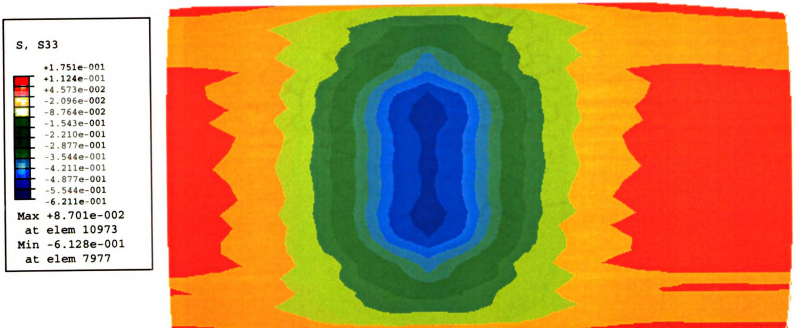

Figure 4.13 Normal stress contour at pressure of 90 psi and deflection of 9.6 mm (6899 N)

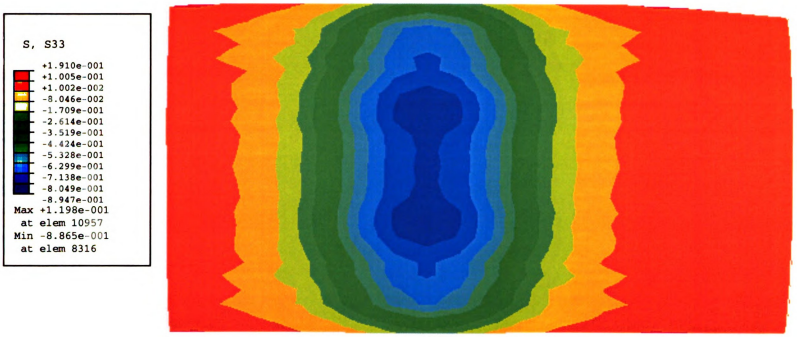

Figure 4.14 Normal stress contour at pressure of 90 psi and deflection of 17.6 mm (13899 N)

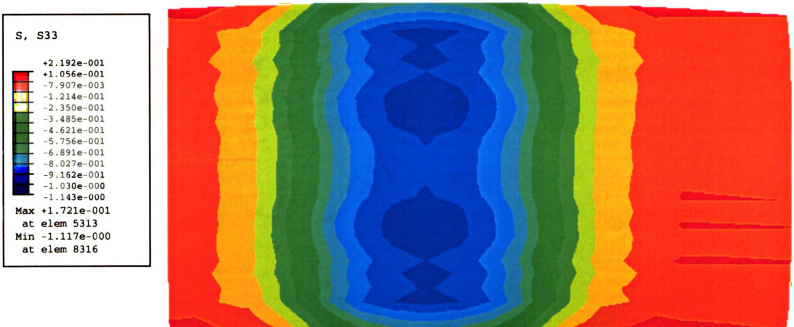

Figure 4.15 Normal stress contour at pressure of 90 psi and deflection of 28.3 mm (25302 N)

Figure 4.16 Normal stress contour at pressure of 90 psi and deflection of 45.2 mm (43120 N)

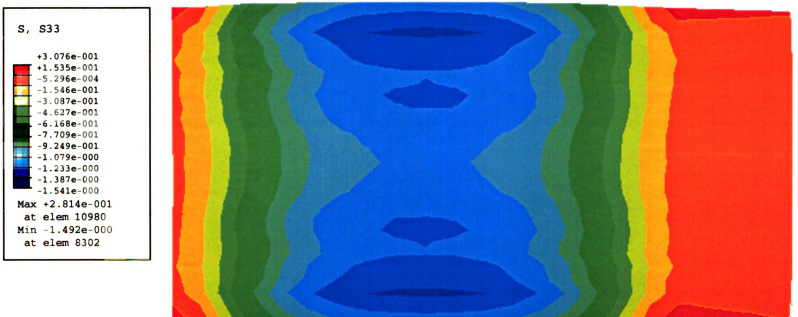

Figure 4.17 Normal stress contour at pressure of 90 psi and deflection of 49.6 mm (47797 N)

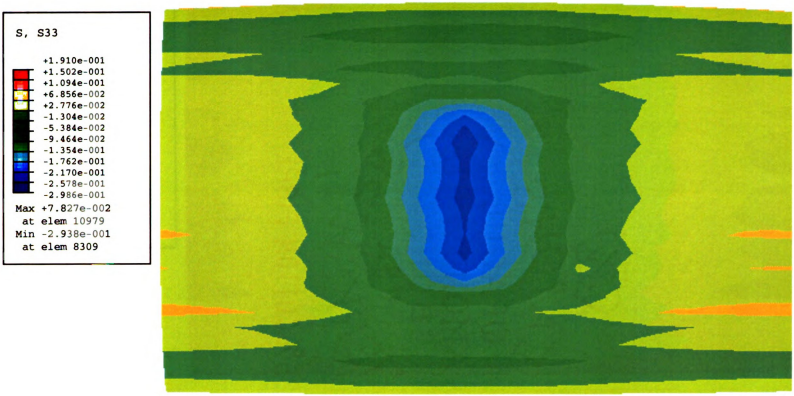

Figure 4.18 Normal stress contour at pressure of 100 psi and deflection of 3.9 mm (2379 N)

Figure 4.19 Normal stress contour at pressure of 100 psi and deflection of 8.4 mm (6624 N)

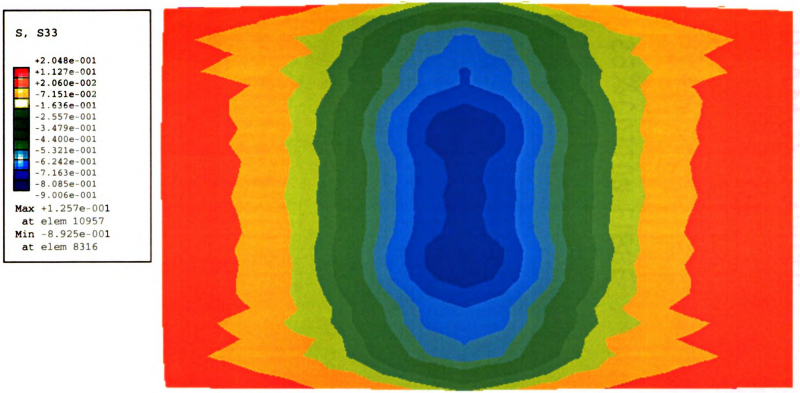

Figure 4.20 Normal stress contour at pressure of 100 psi and deflection of 16.4 mm (13953 N)

Figure 4.21 Normal stress contour at pressure of 100 psi and deflection of 27.7 mm (25961 N)

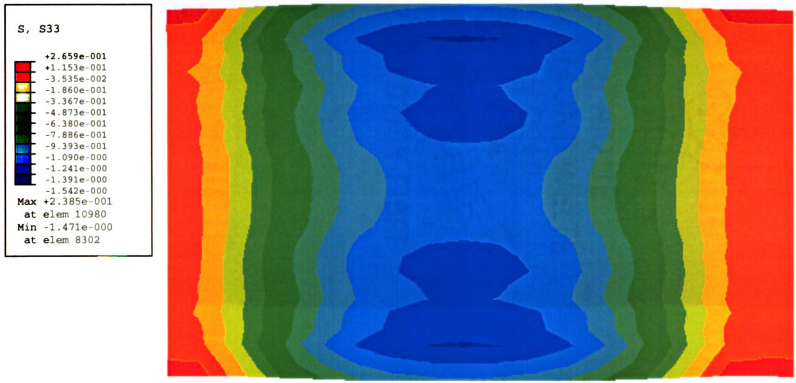

Figure 4.22 Normal stress contour at pressure of 100 psi and deflection of 44.6 mm (44688 N)

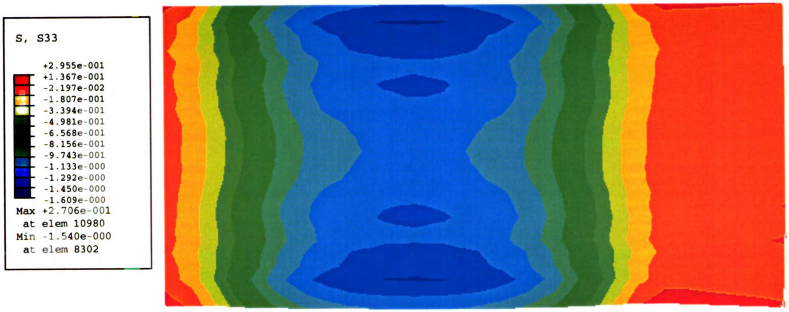

Figure 4.23 Normal stress contour at pressure of 100 psi and deflection of 48.9 mm (49613 N)

Figure 4.24 Normal stress contour at pressure of 110 psi and deflection of 6.8 mm (4961 N)

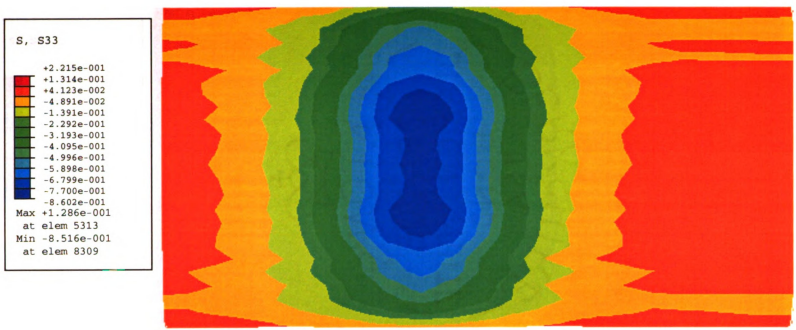

Figure 4.25 Normal stress contour at pressure of 110 psi and deflection of 14.6 mm (12909 N)

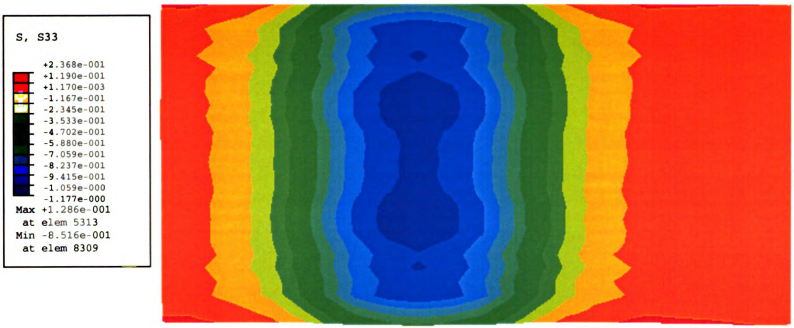

Figure 4.26 Normal stress contour at pressure of 110 psi and deflection of 26.3 mm (26379 N)

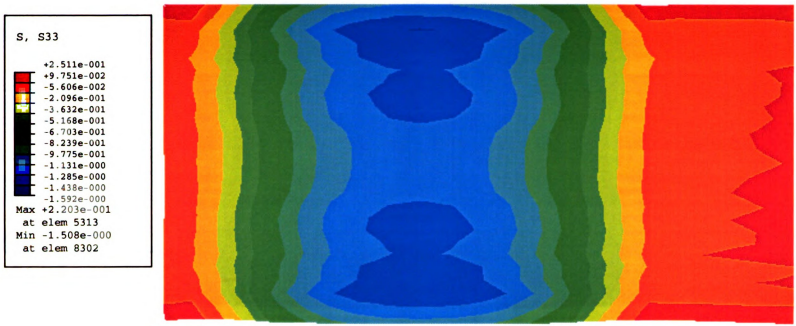

Figure 4.27 Normal stress contour at pressure of 110 psi and deflection of 43.8 mm (47726 N)

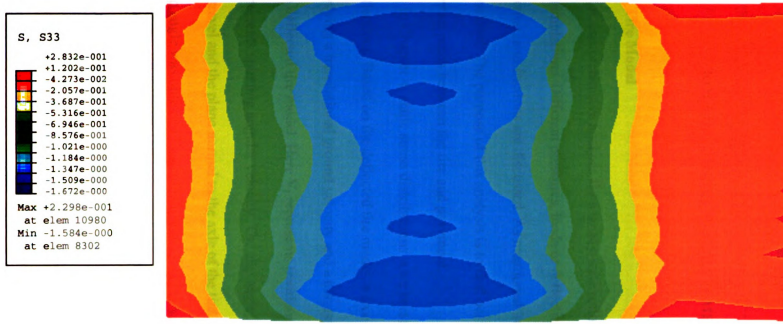

Figure 4.28 Normal stress contour at pressure of 110 psi and deflection of 48.4 mm (53372 N)

Chapter 5

ROLLING TRUCK TIRE/PAVEMENT INTERACTIONS

5.1 Tire Model

A comprehensive analysis for a steady-state rolling truck tire is completed by a series of simulations. Different pressures, loads or deflections, speeds, slip angles, braking or traction, and frictions are discussed. As mentioned in the Chapter 4, a rigid pavement is simulated. The purpose of this analysis is to find out the effects of these factors on the contact patch between the tire and pavement.

In Chapter 4, static stress distributions were presented for given pressures and deflections. Based on the deflected tire model, a free rolling tire model was obtained by applying a translational ground velocity and a corresponding spinning angular velocity on the deflected tire model. Here V_t represents translational ground velocity and V_ω represents spinning angular velocity. The slip angle, θ, is the angle between the direction of travel and the plane normal to the axle of the tire. A free rolling model with different slip angle was obtained by gradually changing the velocity angle of the free rolling model. A traction or braking model was obtained by changing the moving ground speed of the free rolling model.

5.2 Simulation results

As with the static analysis, three tire pressures were considered: 90psi, 100psi, and 110psi. The detail information of simulations is listed in Table 5.1, Table 5.2, and Table 5.3 for the three pressure levels, respectively. For each simulation the contact stress distributions were obtained. Summaries of the results of these simulations are listed in Table 5.4, Table 5.5, and Table 5.6 for free rolling, traction or braking, and slip angle respectively. Figures 5.1 to 5.34 show detailed contact stress plots that are keyed to the simulation cases summarized in Table 5.4 to 5.6.

Table 5.1 Detail information for tire of 90psi

Simulation case	Detail information
P90_Free_1	Defl. = 22 mm, Friction = 0.95, v=5 mph, free rolling
P90_Free_2	Defl. = 42 mm, Friction = 0.95, v=5 mph, free rolling
P90_Free_3	Defl. = 50 mm, Friction = 0.95, v=65 mph, free rolling
P90_Slip_1	Defl. = 50 mm, Friction = 1.0, v=65 mph, slip angle =1.5^0
P90_Slip_2	Defl. = 50 mm, Friction = 1.0, v=65 mph, slip angle =2.4^0
P90_Slip_3	Defl. = 50 mm, Friction = 1.0, v=65 mph, slip angle =3.0^0
P90_Slip_4	Defl. = 50 mm, Friction = 0.9, v=65 mph, slip angle =1.5^0
P90_Slip_5	Defl. = 50 mm, Friction = 0.9, v=65 mph, slip angle =2.4^0
P90_Slip_6	Defl. = 50 mm, Friction = 0.9, v=65 mph, slip angle =3.0^0
P90_Tr_1	Defl. = 50 mm, Friction = 0.95, V_t=65 mph, V_r=70 mph, Traction
P90_Tr_2	Defl. = 50 mm, Friction = 0.95, V_t=65 mph, V_r=75 mph, Traction
P90_Bk_1	Defl. = 50 mm, Friction = 0.95, V_t=65 mph, V_r=60 mph, Braking
P90_Bk_2	Defl. = 50 mm, Friction = 0.95, V_t=65 mph, V_r=55 mph, Braking

Table 5.2 Detail information for tire of 100psi

Simulation case	Detail information
P100_Free_1	Defl. = 29 mm, Friction = 0.95, v=65 mph, free rolling
P100_Free_2	Defl. = 50 mm, Friction = 0.95, v=45 mph, free rolling
P100_Free_3	Defl. = 50 mm, Friction = 0.95, v=65 mph, free rolling
P100_Slip_1	Defl. = 29 mm, Friction = 0.95, v=65 mph, slip angle =0.9^0
P100_Slip_2	Defl. = 29 mm, Friction = 0.95, v=65 mph, slip angle =1.8^0
P100_Slip_3	Defl. = 29 mm, Friction = 0.95, v=65 mph, slip angle =3.0^0
P100_Slip_4	Defl. = 50 mm, Friction = 0.95, v=45 mph, slip angle =1.5^0
P100_Slip_5	Defl. = 50 mm, Friction = 0.95, v=45 mph, slip angle =3.0^0
P100_Slip_6	Defl. = 50 mm, Friction = 0.95, v=65 mph, slip angle =0.9^0
P100_Slip_7	Defl. = 50 mm, Friction = 0.95, v=65 mph, slip angle =1.8^0
P100_Slip_8	Defl. = 50 mm, Friction = 0.95, v=65 mph, slip angle =3.0^0
P100_Tr_1	Defl. = 29 mm, Friction = 0.95, V_t=65 mph, V_r=68.5 mph, Traction
P100_Tr_2	Defl. = 29 mm, Friction = 0.95, V_t=65 mph, V_r=74.1 mph, Traction
P100_Tr_3	Defl. = 50 mm, Friction = 0.95, V_t=65 mph, V_r=70 mph, Traction
P100_Tr_4	Defl. = 50 mm, Friction = 0.95, V_t=65 mph, V_r=75 mph, Traction

Table 5.3 Detail information for tire of 110psi

Simulation case	Detail information
P110_Free_1	Defl. = 50 mm, Friction = 0.95, v=65 mph, free rolling
P110_Slip_1	Defl. = 50 mm, Friction = 0.95, v=65 mph, slip angle =0.9^0
P110_Slip_2	Defl. = 50 mm, Friction = 0.95, v=65 mph, slip angle =1.8^0
P110_Slip_3	Defl. = 50 mm, Friction = 0.95, v=65 mph, slip angle =3.0^0
P110_Tr_1	Defl. = 50 mm, Friction = 0.95, V_t=65 mph, V_r=70 mph, Traction
P110_Tr_2	Defl. = 50 mm, Friction = 0.95, V_t=65 mph, V_r=75 mph, Traction

Table 5.4 Results for Free Rolling

Simulation case	Pressure (psi)	Deflection (mm)	Speed (mph)	Max. $\|\sigma_{33}\|$ (Mpa)	Max. $\|\sigma_{31}\|$ (Mpa)	Contact area (mm^2)	Figure No.
P90_Free_1	90	22	5	1.012	0.2322	35604	Fig. 5-1
P90_Free_2	90	42	5	1.421	0.31	55265	Fig. 5-2
P90_Free_3	90	50	65	1.481	0.2948	62485	Fig. 5-3
P100_Free_1	100	29	65	1.228	0.2506	39304	Fig. 5-4
P100_Free_2	100	50	45	1.548	0.2928	61147	Fig. 5-5
P100_Free_3	100	50	65	1.628	0.3587	61473	Fig. 5-6
P110_Free_1	110	50	65	1.694	0.3623	60048.	Fig. 5-7

Table 5.5 Results for Traction and Braking

Simulation case	Pressure (psi)	Deflection (mm)	V_t/ V_r	Max. $\|\sigma_{33}\|$ (Mpa)	Max. $\|\sigma_{31}\|$ (Mpa)	Contact area (mm^2)	Figure No.
P90_Tr_1	90	50	65/70	1.625	1.215		Fig. 5-8
P90_Tr_2	90	50	65/75	1.812	1.291	64467	Fig. 5-9
P90_Bk_1	90	50	65/60	1.961	1.336		Fig. 5-10
P90_Bk_2	90	50	65/55	2.442	1.609	63024	Fig. 5-11
P100_Tr_1	100	29	65/68.5	1.666	0.8		Fig. 5-12
P100_Tr_2	100	29	65/74.1	1.515	0.9745	43150	Fig. 5-13
P100_Tr_3	100	50	65/70	2.096	1.313		Fig. 5-14
P100_Tr_4	100	50	65/75	1.808	1.401	64482	Fig. 5-15
P110_Tr_1	110	50	65/70	2.194	1.361		Fig. 5-16
P110_Tr_2	110	50	65/75	1.893	1.456	68480	Fig. 5-17

Table 5.6 Results for Slip Rolling

Simulation case	Pressure (psi)	Defl. (mm)	Speed (mph)	Slip angle (Degree)	Max. $\|\sigma_{33}\|$ (Mpa)	Max. $\|\sigma_{31}\|$ (Mpa)	Max. $\|\sigma_{32}\|$ (Mpa)	Contact area (mm^2)	Figure No.
P90_Slip_1	90	50	65	1.5	1.968	0.3835	0.4734		Fig. 5-18
P90_Slip_2	90	50	65	2.4	2.031	0.4921	0.6887		Fig. 5-19
P90_Slip_3	90	50	65	3.0	2.631	0.5858	0.6934	58399	Fig. 5-20
P90_Slip_4	90	50	65	1.5	1.973	0.3924	0.4692		Fig. 5-21
P90_Slip_5	90	50	65	2.4	2.085	0.4927	0.7045		Fig. 5-22
P90_Slip_6	90	50	65	3.0	2.546	0.5885	0.7331	58544	Fig. 5-23
P100_Slip_1	100	29	65	0.9	1.275	0.2704	0.1923		Fig. 5-24
P100_Slip_2	100	29	65	1.8	1.332	0.3137	0.3131		Fig. 5-25
P100_Slip_3	100	29	65	3.0	1.74	0.3982	0.6956	38318	Fig. 5-26
P100_Slip_4	100	50	45	1.5	2.231	0.3894	0.5952		Fig. 5-27
P100_Slip_5	100	50	45	3.0	2.488	0.5907	0.8206	57690	Fig. 5-28
P100_Slip_6	100	50	65	0.9	1.745	0.3976	0.331		Fig. 5-29
P100_Slip_7	100	50	65	1.8	2.296	0.4614	0.7459		Fig. 5-30
P100_Slip_8	100	50	65	3.0	2.964	0.7741	0.1658	56188	Fig. 5-31

Table 5.6 (cont'd).

Simulation case	Pressure (psi)	Defl. (mm)	Speed (mph)	Slip angle (Degree)	Max. $\|\sigma_{33}\|$ (Mpa)	Max. $\|\sigma_{31}\|$ (Mpa)	Max. $\|\sigma_{32}\|$ (Mpa)	Contact area (mm^2)	Figure No.
P110_Slip_1	110	50	65	0.9	1.767	0.3807	0.3349		Fig. 5-32
P110_Slip_2	110	50	65	1.8	2.425	0.4596	0.7246		Fig. 5-33
P110_Slip_3	110	50	65	3.0	2.713	0.8851	1.172	57492	Fig. 5-34

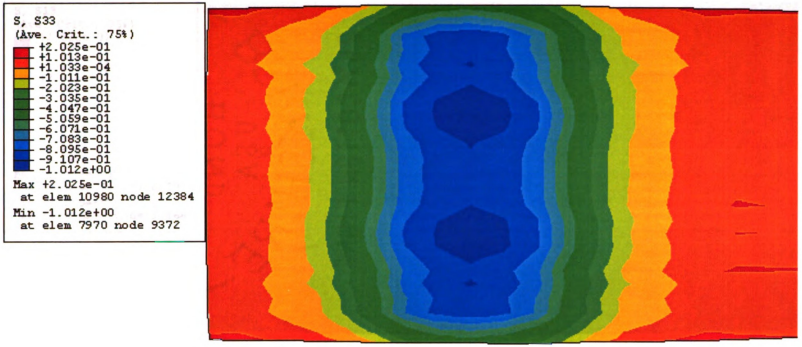

Figure 5.1a Normal stress contour for a free rolling
at pressure of 90 psi, deflection of 22. mm (18871. N), friction of 0.95, and velocity of 5 mph

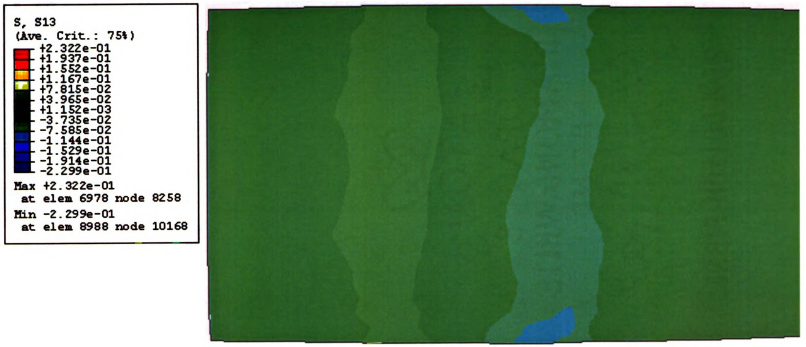

Figure 5.1b Shear stress contour (xz) for a free rolling
at pressure of 90 psi, deflection of 22. mm (188871. N), friction of 0.95, and velocity of 5 mph

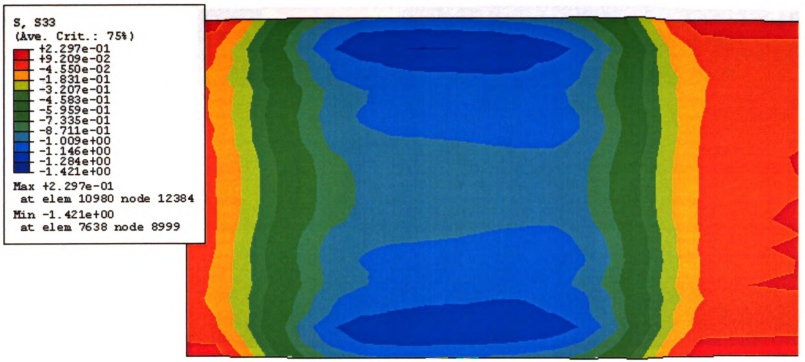

Figure 5.2a Normal stress contour for a free rolling
at pressure of 90 psi, deflection of 42.2 mm (40000.0 N), friction of 0.95, and velocity of 5 mph

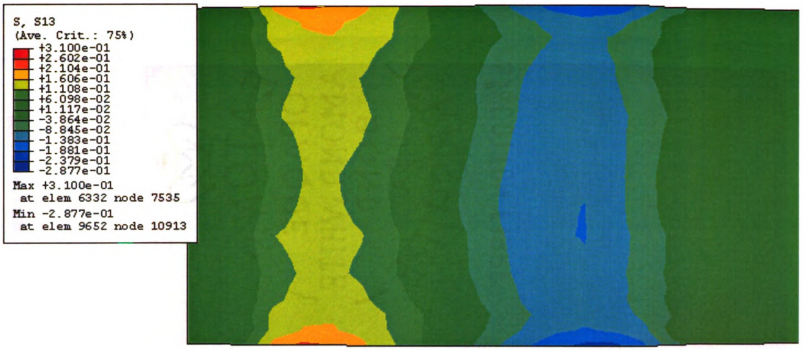

Figure 5.2b Shear stress contour (xz) for a free rolling
at pressure of 90 psi, deflection of 42.2 mm (40000.0 N), friction of 0.95, and velocity of 5 mph

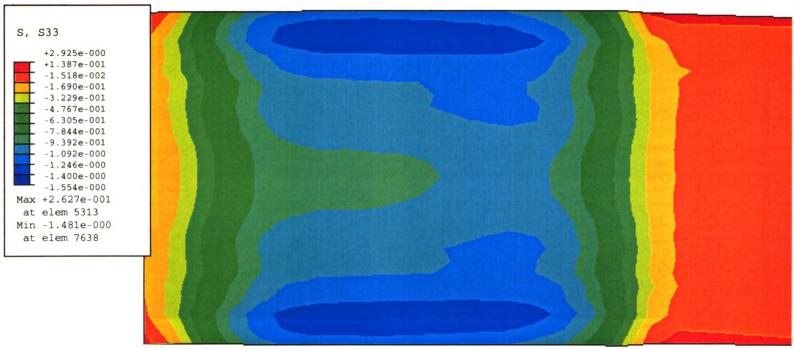

Figure 5.3a Normal stress contour for a free rolling
at pressure of 90 psi, deflection of 49.6 mm (47797 N), friction of 0.95, and velocity of 65 mph

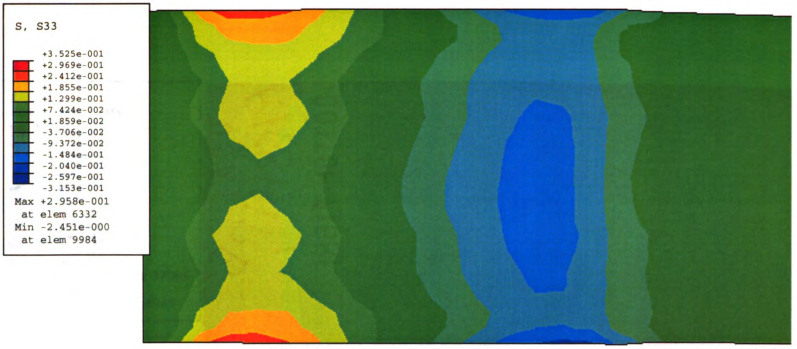

Figure 5.3b Shear stress contour (xz) for a free rolling
at pressure of 90 psi, deflection of 49.6 mm (47797 N), friction of 0.95, and velocity of 65 mph

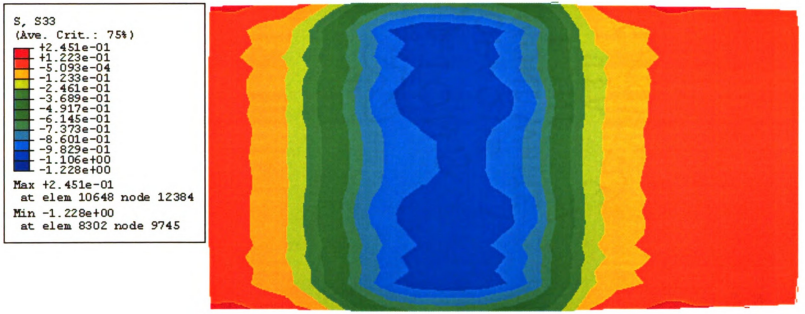

Figure 5.4a Normal stress contour for a free rolling
at pressure of 100 psi, deflection of 29 mm (26414 N), friction of 0.95, and velocity of 65 mph

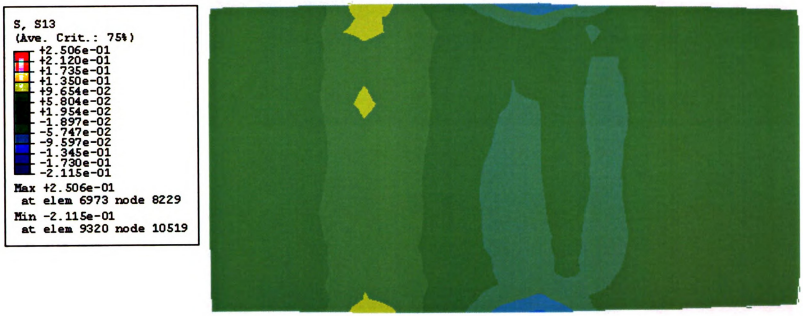

Figure 5.4b Shear stress contour (xz) for a free rolling
at pressure of 100 psi, deflection of 29 mm (26414 N), friction of 0.95, and velocity of 65 mph

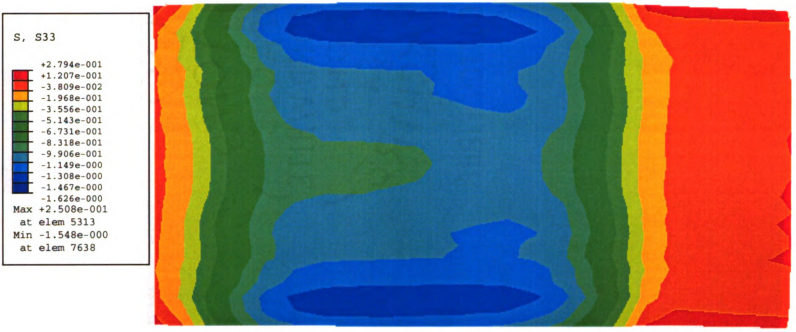

Figure 5.5a Normal stress contour for a free rolling
at pressure of 100 psi, deflection of 48.9 mm (49613 N), friction of 0.95, and velocity of 45 mph

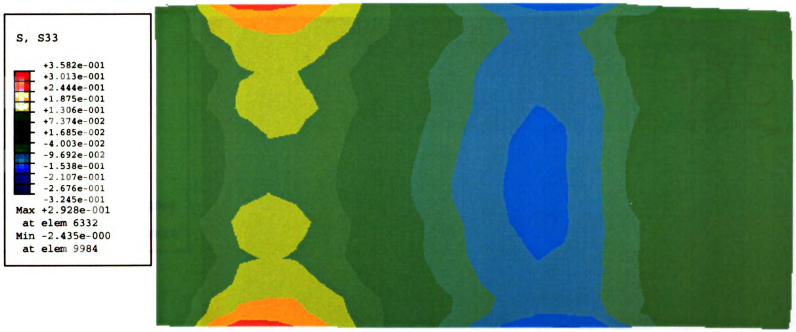

Figure 5.5b Shear stress contour (xz) for a free rolling
at pressure of 100 psi, deflection of 48.9 mm (49613 N), friction of 0.95, and velocity of 45 mph

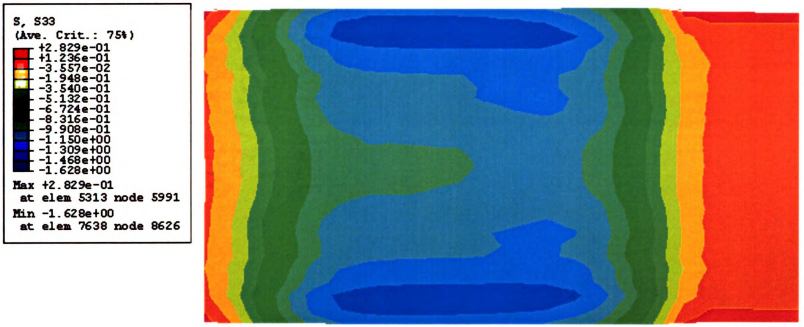

Figure 5.6a Normal stress contour for a free rolling
at pressure of 100 psi, deflection of 48.9 mm (49613 N), friction of 0.95, and velocity of 65 mph

Figure 5.6b Shear (xz) stress contour for a free rolling
at pressure of 100 psi, deflection of 48.9 mm (49613 N), friction of 0.95, and velocity of 65 mph

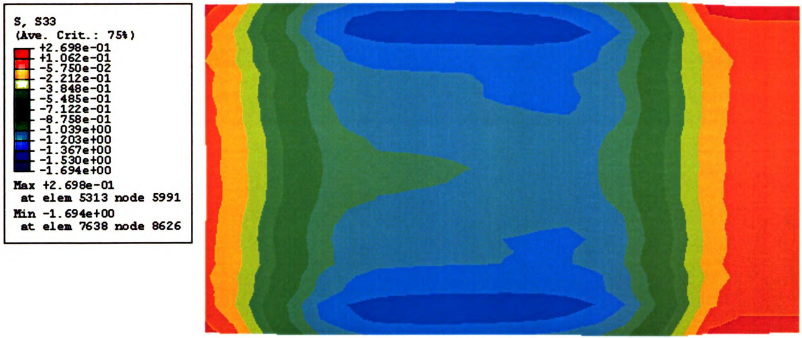

Figure 5.7a Normal stress contour for a free rolling
at pressure of 110 psi, deflection of 48.4 mm (53372 N), friction of 0.95, and velocity of 65 mph

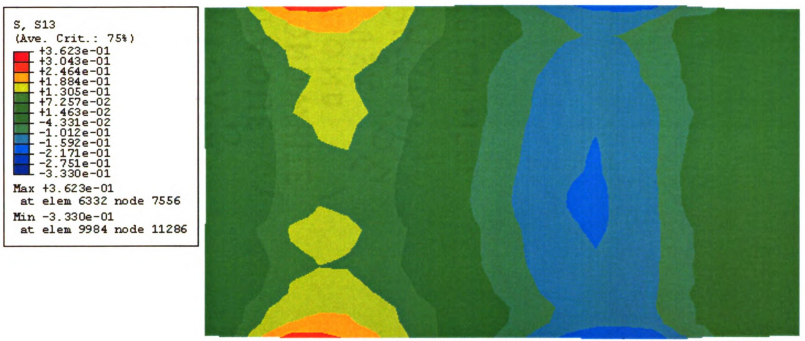

Figure 5.7b Shear stress contour (xz) for a free rolling
at pressure of 110 psi, deflection of 48.4 mm (53372 N), friction of 0.95, and velocity of 65 mph

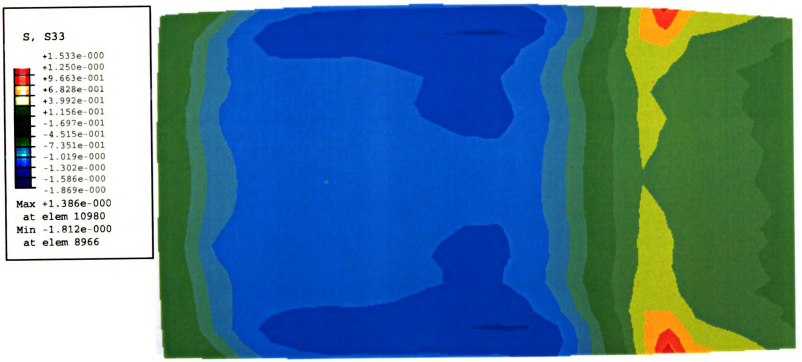

Figure 5.8a Normal stress contour for a traction
at pressure of 90 psi, deflection of 49.6 mm (47797 N), friction of 0.95, v_t = 65 mph, v_r= 70 mph

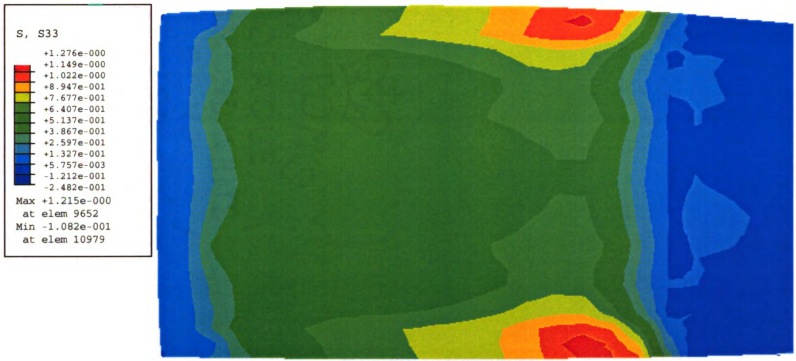

Figure 5.8b Shear stress contour (xz) for a traction
at pressure of 90 psi, deflection of 49.6 mm (47797 N), friction of 0.95, v_t = 65 mph, v_r= 70 mph

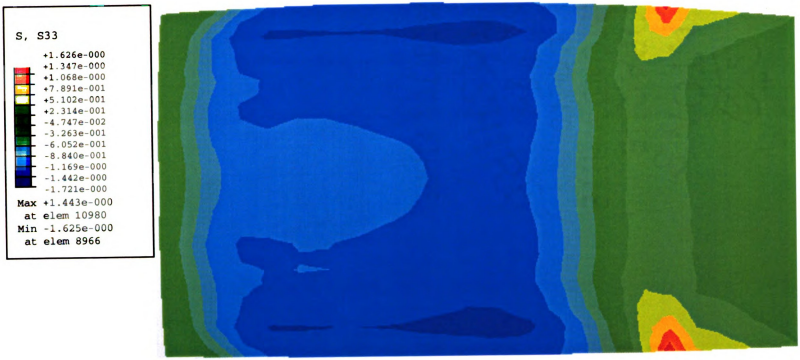

Figure 5.9a Normal stress contour for a traction
at pressure of 90 psi, deflection of 49.6 mm (47797 N), friction of 0.95, v_t = 65 mph, v_r= 75 mph

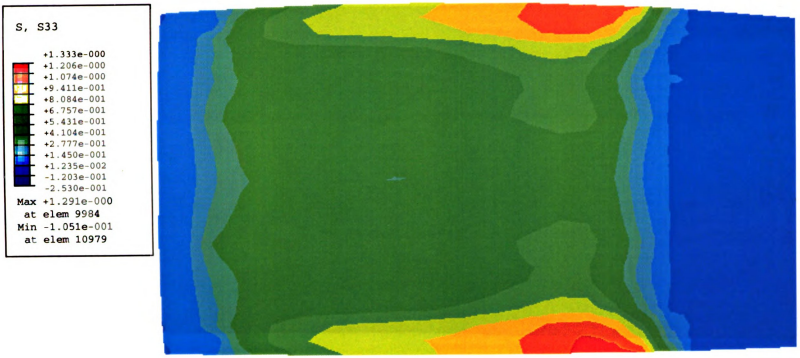

Figure 5.9b Shear stress contour (xz) for a traction
at pressure of 90 psi, deflection of 49.6 mm (47797 N), friction of 0.95, v_t = 65 mph, v_r= 75 mph

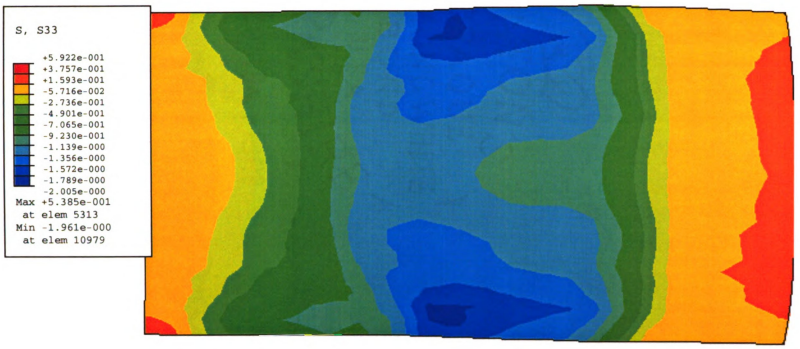

Figure 5.10a Normal stress contour for a braking
at pressure of 90 psi, deflection of 49.6 mm (47797 N), friction of 0.95, v_t = 65 mph, v_f= 60 mph

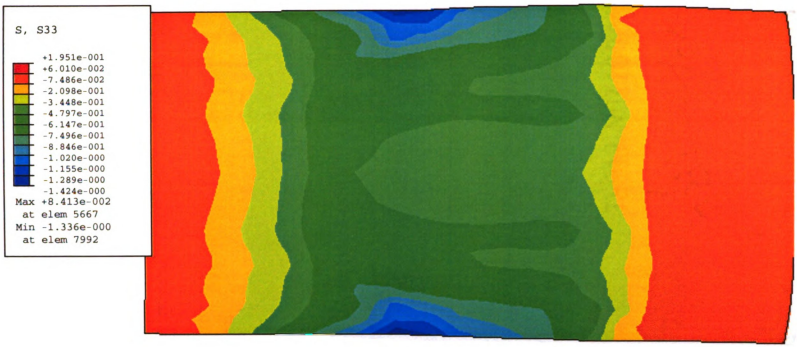

Figure 5.10b Shear stress contour (xz) for a braking
at pressure of 90 psi, deflection of 49.6 mm (47797 N), friction of 0.95, v_t = 65 mph, v_r= 60 mph

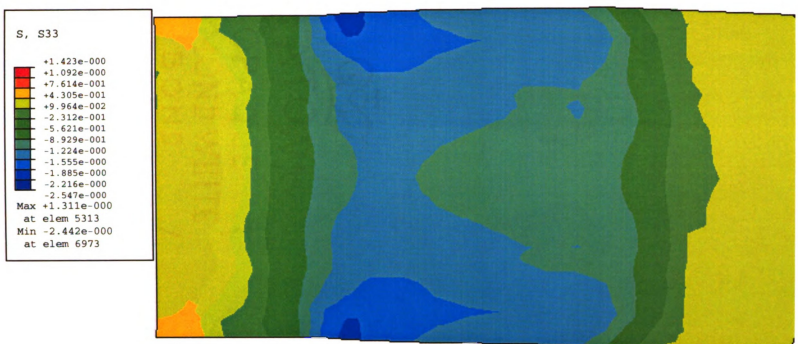

Figure 5.11a Normal stress contour for a braking
at pressure of 90 psi, deflection of 49.6 mm (47797 N), friction of 0.95, v_t = 65 mph, v_r= 55 mph

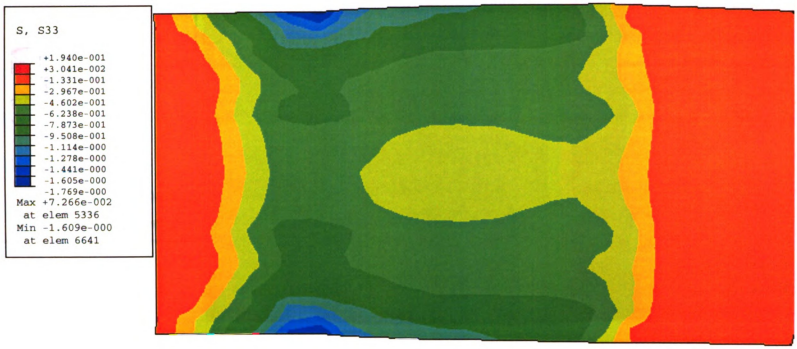

Figure 5.11b Shear stress contour (xz) for a braking
at pressure of 90 psi, deflection of 49.6 mm (47797 N), friction of 0.95, v_t = 65 mph, v_r= 55 mph

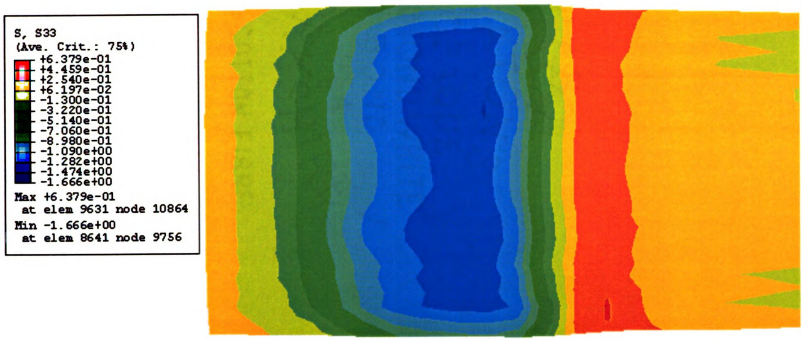

Figure 5.12a Normal stress contour for a traction
at pressure of 100 psi, deflection of 29 mm (26414 N), friction of 0.95, v_t = 65 mph, v_r= 68.5 mph

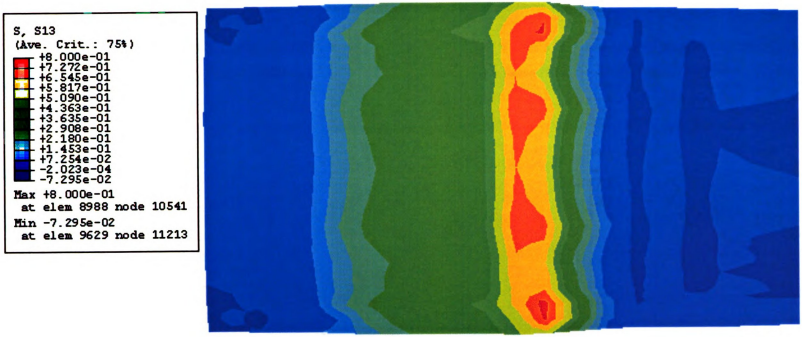

Figure 5.12b Shear stress contour (xz) for a traction
at pressure of 100 psi, deflection of 29 mm (26414 N), friction of 0.95, v_t = 65 mph, v_r= 68.5 mph

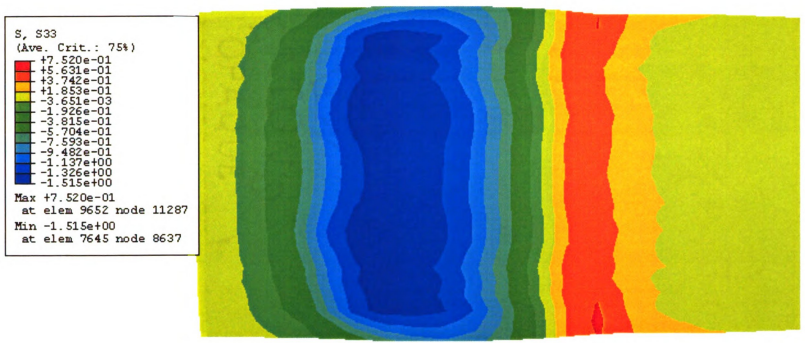

Figure 5.13a Normal stress contour for a traction
at pressure of 100 psi, deflection of 29 mm (26414 N), friction of 0.95, v_t = 65 mph, v_r= 74.1 mph

Figure 5.13b Shear stress contour (xz) for a traction
at pressure of 100 psi, deflection of 29 mm (26414 N), friction of 0.95, v_t = 65 mph, v_r= 74.1 mph

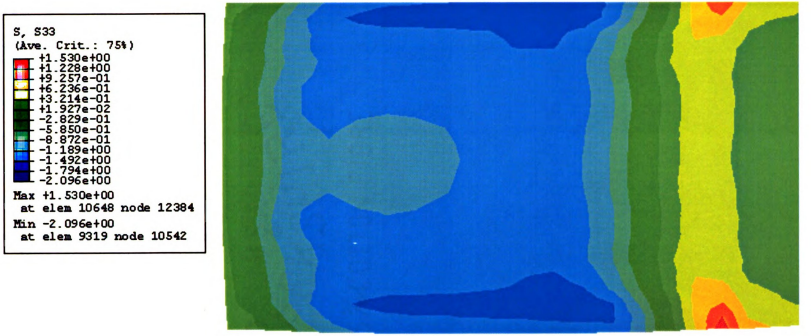

Figure 5.14a Normal stress contour for a traction
at pressure of 100 psi, deflection of 48.9 mm (49613 N), friction of 0.95, v_t = 65 mph, v_r= 70 mph

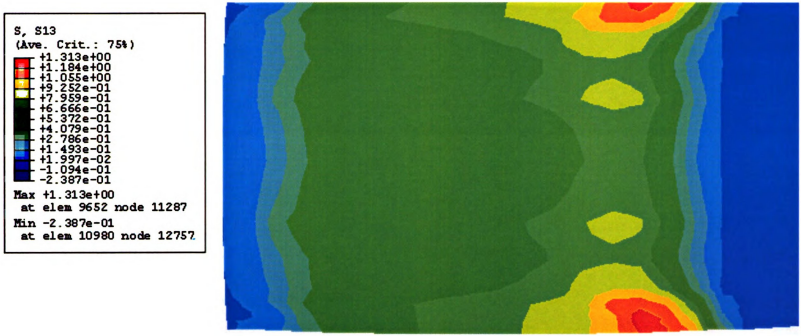

Figure 5.14b Shear stress contour (xz) for a traction
at pressure of 100 psi, deflection of 48.9 mm (49613 N), friction of 0.95, v_t = 65 mph, v_r= 70 mph

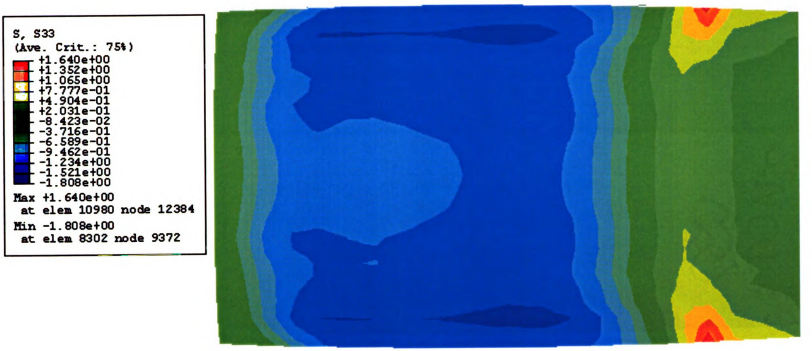

Figure 5.15a Normal stress contour for a traction
at pressure of 100 psi, deflection of 48.9 mm (49613 N), friction of 0.95, v_t = 65 mph, v_r= 75 mph

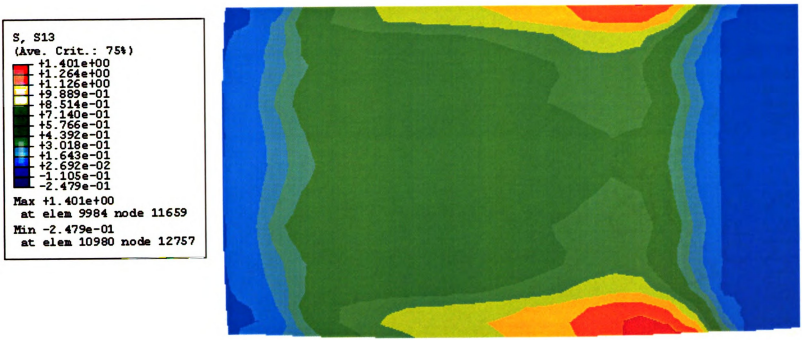

Figure 5.15b Shear stress contour (xz) for a traction
at pressure of 100 psi, deflection of 48.9 mm (49613 N), friction of 0.95, v_t = 65 mph, v_r= 75 mph

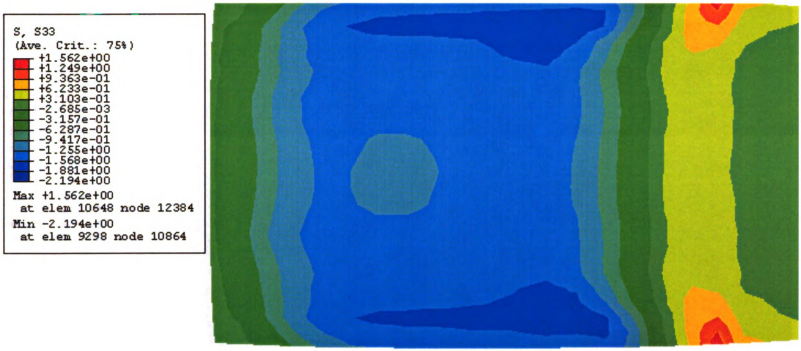

Figure 5.16a Normal stress contour for a traction
at pressure of 110 psi, deflection of 48.4 mm (53372 N), friction of 0.95, v_t = 65 mph, v_r= 70 mph

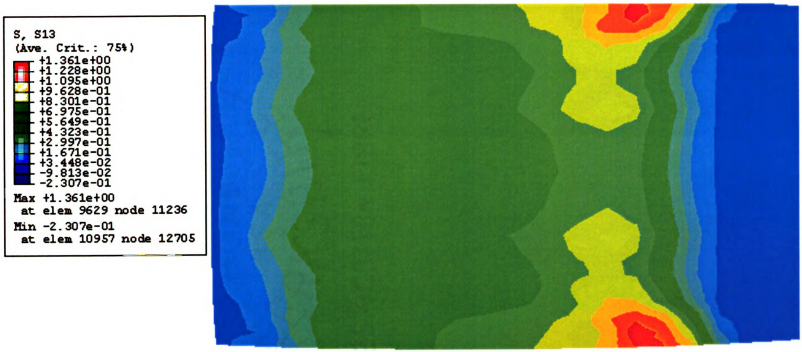

Figure 5.16b Shear stress contour (xz) for a traction
at pressure of 110 psi, deflection of 48.4 mm (53372 N), friction of 0.95, v_t = 65 mph, v_r= 70 mph

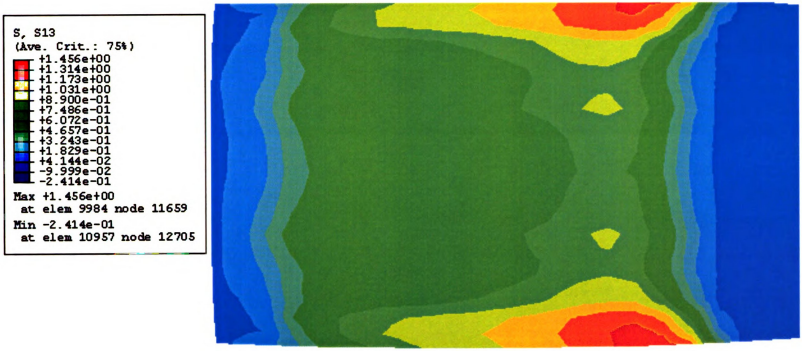

Figure 5.17a Normal stress contour for a traction
at pressure of 110 psi, deflection of 48.4 mm (53372 N), friction of 0.95, v_t = 65 mph, v_r= 75 mph

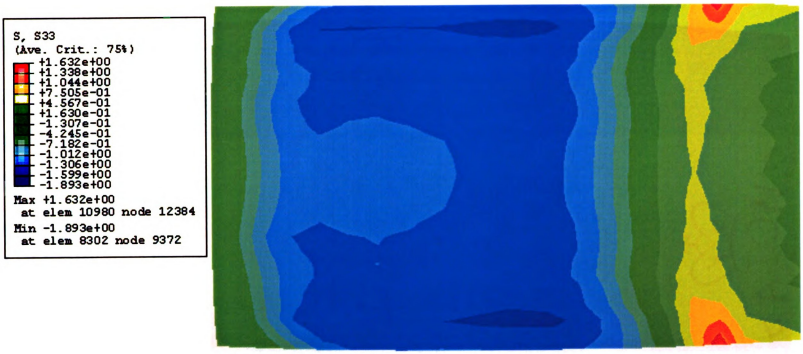

Figure 5.17b Shear stress contour (xz) for a traction
at pressure of 110 psi, deflection of 48.4 mm (53372 N), friction of 0.95, v_t = 65 mph, v_r= 75 mph

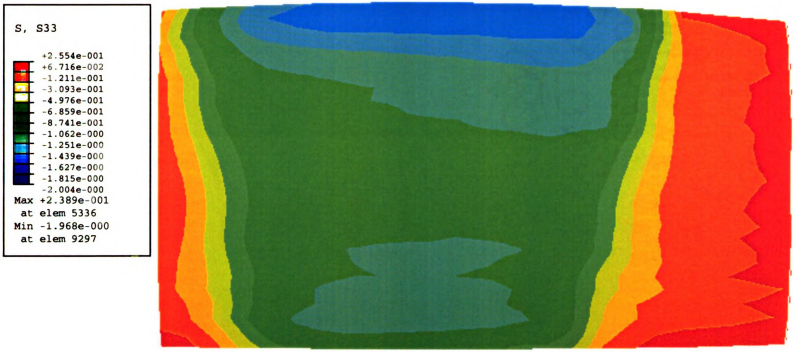

Figure 5.18a Normal stress contour for a slip
at pressure of 90 psi, deflection of 49.6 mm (47797 N), friction of 1.0, v_t = 65 mph, slip angle = 1.5^0

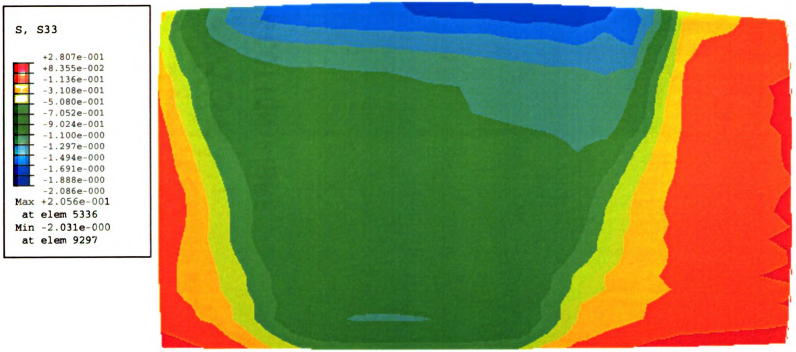

Figure 5.19a Normal stress contour for a slip
at pressure of 90 psi, deflection of 49.6 mm (47797 N), friction of 1.0, v_t = 65 mph, slip angle = 2.4^0

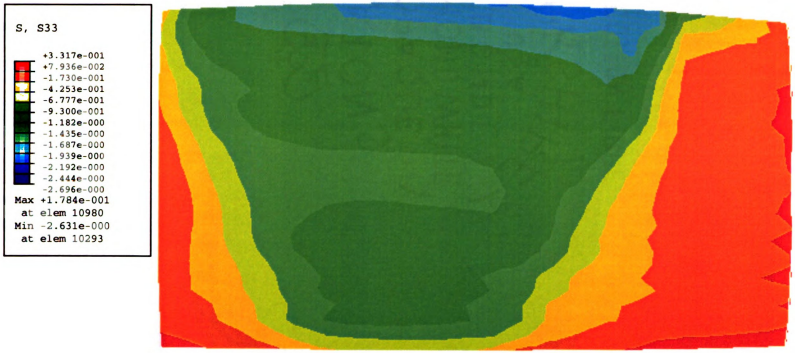

Figure 5.20a Normal stress contour for a slip
at pressure of 90 psi, deflection of 49.6 mm (47797 N), friction of 1.0, v_t = 65 mph, slip angle = 3.0^0

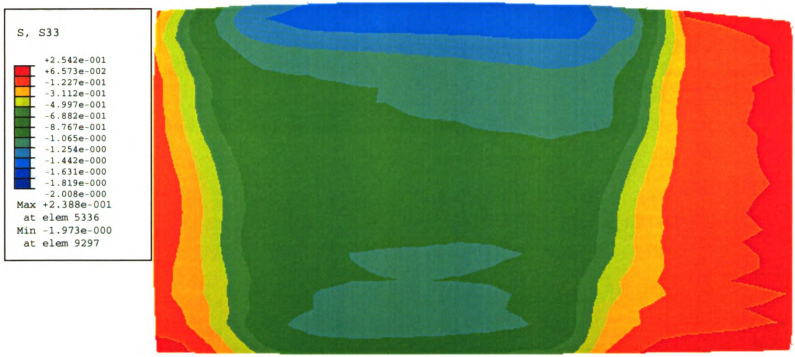

Figure 5.21a Normal stress contour for a slip
at pressure of 90 psi, deflection of 49.6 mm (47797 N), friction of 0.95, v_t = 65 mph, slip angle = 1.5^0

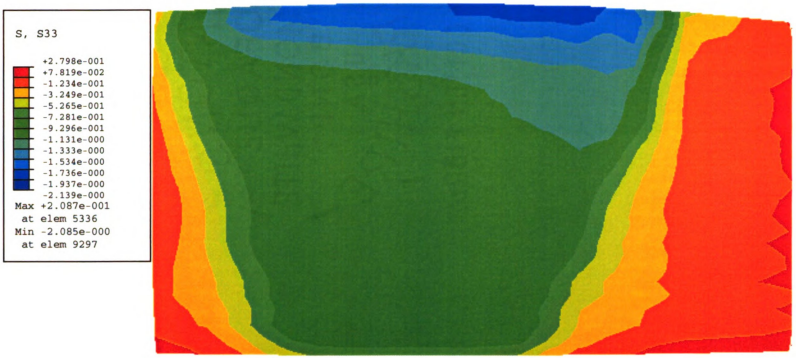

Figure 5.22a Normal stress contour for a slip
at pressure of 90 psi, deflection of 49.6 mm (47797 N), friction of 0.95, v_t = 65 mph, slip angle = 2.4^0

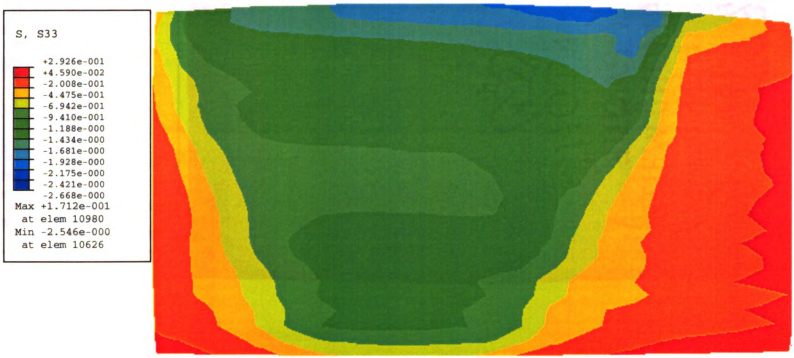

Figure 5.23a Normal stress contour for a slip
at pressure of 90 psi, deflection of 49.6 mm (47797 N), friction of 0.95, v_t = 65 mph, slip angle = 3.0^0

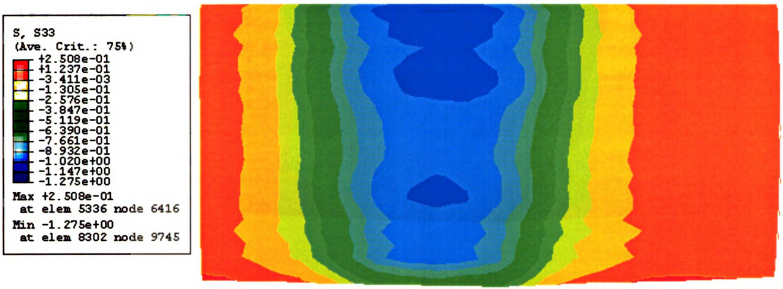

Figure 5.24a Normal stress contour for a slip
at pressure of 100 psi, deflection of 29 mm (26414 N), friction of 0.95, v_t = 65 mph, slip angle = 0.9^0

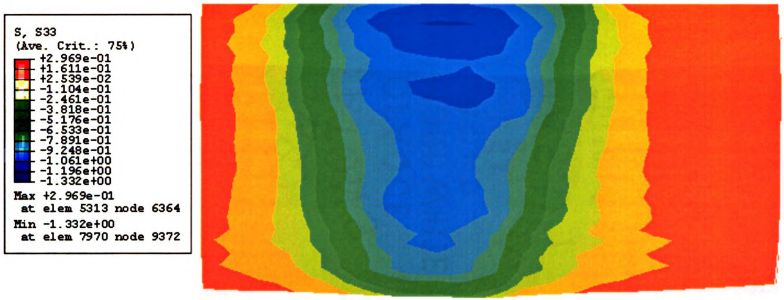

Figure 5.25a Normal stress contour for a slip
at pressure of 100 psi, deflection of 29 mm (26414 N), friction of 0.95, v_t = 65 mph, slip angle = 1.8^0

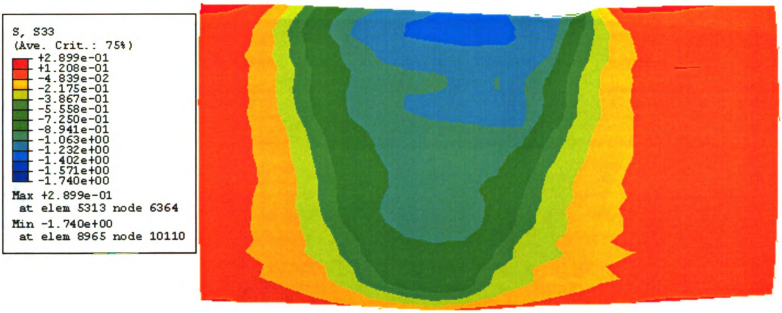

Figure 5.26a Normal stress contour for a slip
at pressure of 100 psi, deflection of 29 mm (26414 N), friction of 0.95, v_t = 65 mph, slip angle = 3.0^0

Figure 5.27a Normal stress contour for a slip
at pressure of 100 psi, deflection of 48.9 mm (49613N), friction of 0.95, v_t = 45 mph, slip angle = 1.5^0

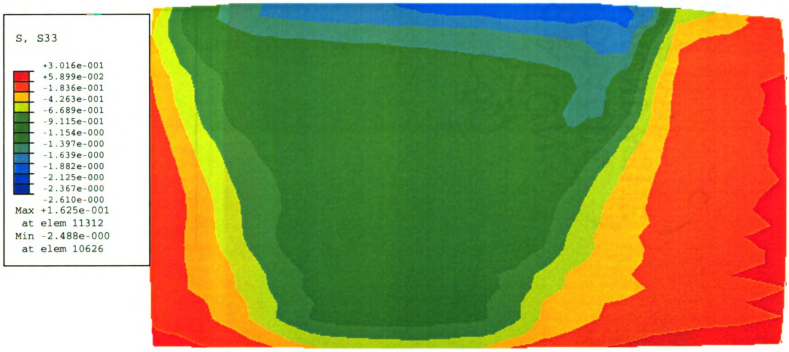

Figure 5.28a Normal stress contour for a slip
at pressure of 100 psi, deflection of 48.9 mm (49613N), friction of 0.95, v_t = 45 mph, slip angle = 3.0^0

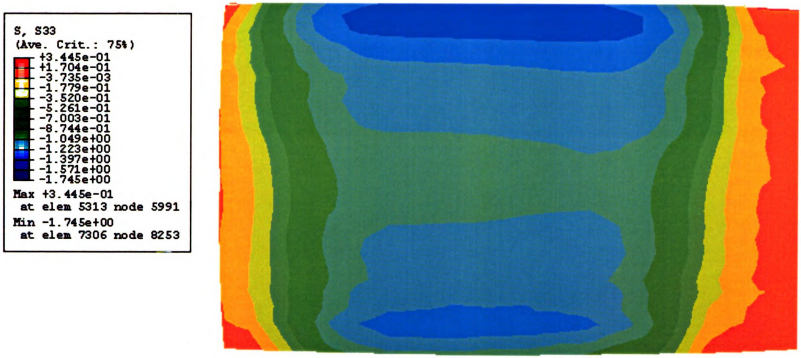

Figure 5.29a Normal stress contour for a slip
at pressure of 100 psi, deflection of 48.9 mm (49613N), friction of 0.95, v_t = 65 mph, slip angle = 0.9^0

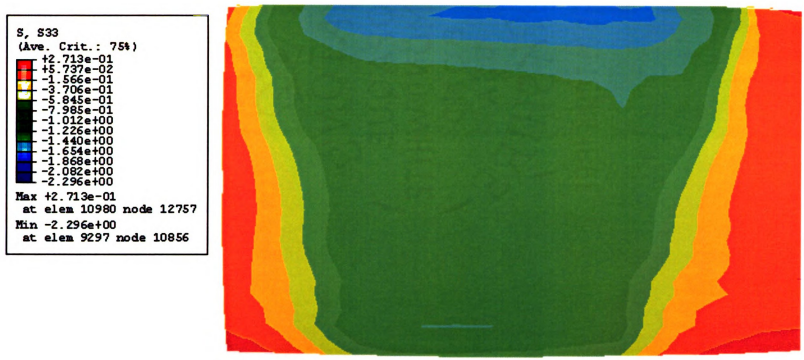

Figure 5.30a Normal stress contour for a slip
at pressure of 100 psi, deflection of 48.9 mm (49613N), friction of 0.95, v_t = 65 mph, slip angle = 1.8^0

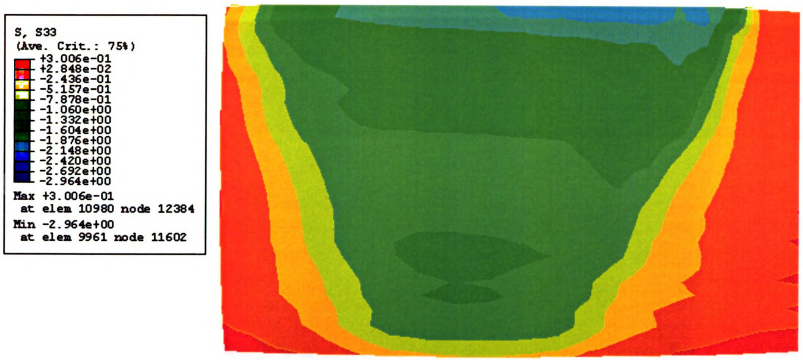

Figure 5.31a Normal stress contour for a slip
at pressure of 100 psi, deflection of 48.9 mm (49613N), friction of 0.95, v_t = 65 mph, slip angle = 3.0^0

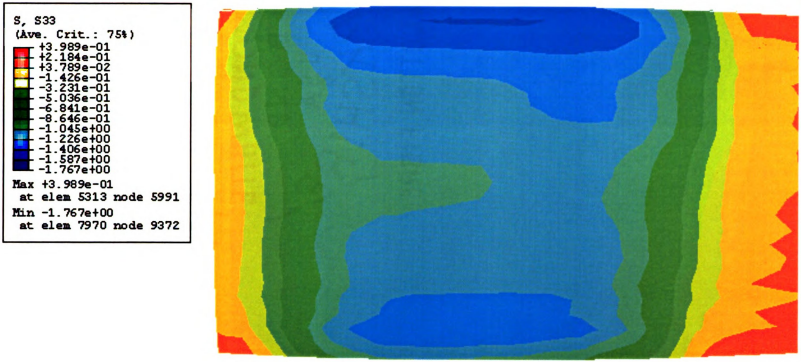

Figure 5.32a Normal stress contour for a slip
at pressure of 110 psi, deflection of 48.4 mm (53372N), friction of 0.95, v_t = 65 mph, slip angle = 0.9^0

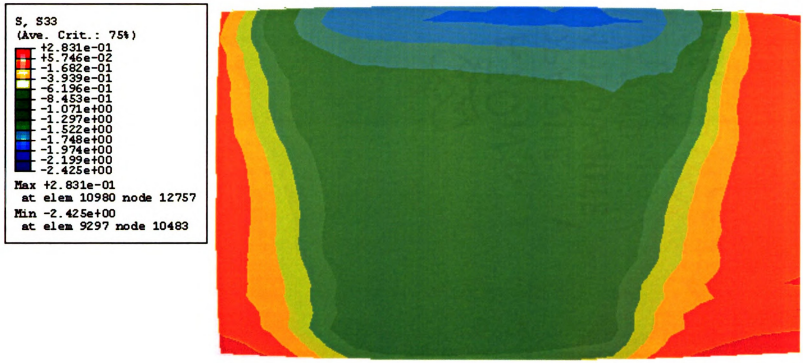

Figure 5.33a Normal stress contour for a slip
at pressure of 110 psi, deflection of 48.4 mm (53372N), friction of 0.95, v_t = 65 mph, slip angle = 1.8^0

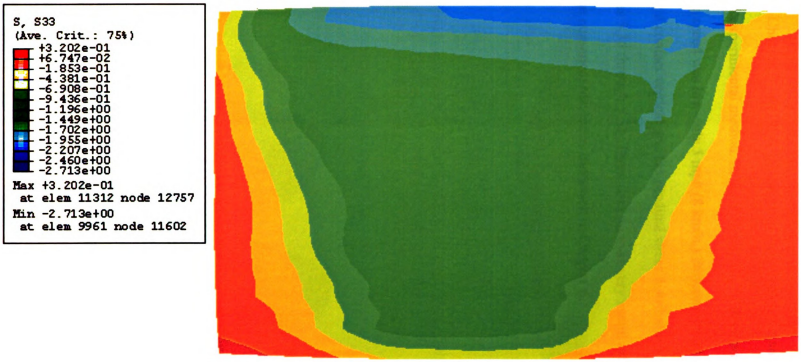

Figure 5.34 Normal stress contour for a slip
at pressure of 110 psi, deflection of 48.4 mm (53372N), friction of 0.95, v_t = 65 mph, slip angle = 3.0^0

5.3 Reference Data for a Slow Rolling Tire Test

As mentioned in Chapter 2, de (1994) investigated the vehicle-road surface contact problem by using an experimental method. In his analysis, a smooth Goodyear tire was used, and the rolling speed was low-only 5 mph (8 km/h.) Different load levels were applied. Some typical contact vertical and longitudinal stress distributions from de's work are shown in Figures 5.35 through 5.38. These data provide very useful information for comparison with the numerical results, as discussed in Chapter 6.

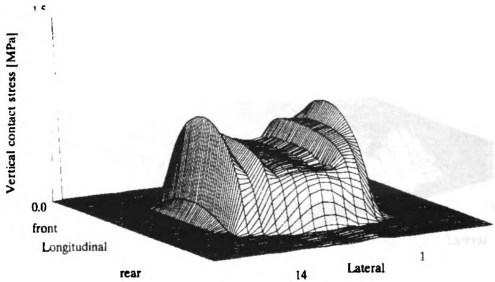

Figure 5.35 Measured vertical stress distribution of 40000. N (8989 lb.) load, tire pressure 90 psi (0.62 Mpa,) and speed of 5 mph (de 1994).

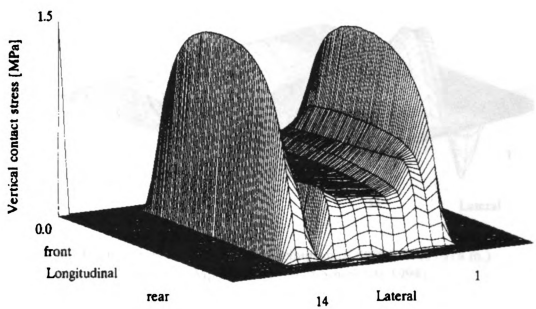

Figure 5.36 Measured vertical stress distribution of 80000. N (17978 lb.) load, tire pressure 90 psi (0.62 Mpa,) and speed of 5 mph (de 1994).

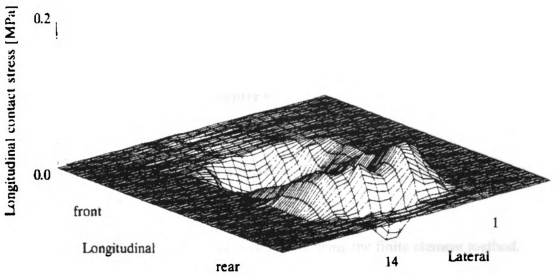

Figure 5.37 Measured longitudinal stress distribution of 40000. N (8989 lb.) load, tire pressure 90 psi (0.62 Mpa,) and speed of 5 mph (de 1994).

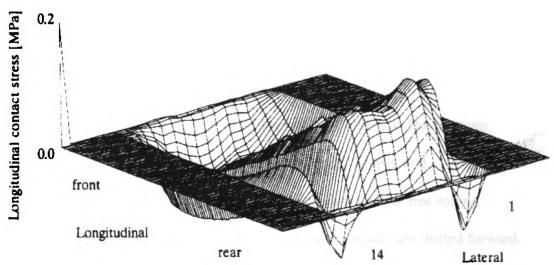

Figure 5.38 Measured longitudinal stress distribution of 80000. N (17978 lb.) load, tire pressure 90 psi (0.62 Mpa,) and speed of 5 mph (de 1994).

Chapter 6

DISCUSSION

The Goodyear 295/75R22.5 truck tire is analyzed by using the finite element method. Different pressures, loads or deflections, speeds, slip angles, braking or traction, and frictions are considered. These data were presented in Chapter 5. As results of a tire rolling over a rigid pavement, these data are very interesting and useful for tire/pavement interaction analysis.

6.1 Free Rolling Tire Model

Results for the free rolling tire model were illustrated in Table 5.4. The pressure levels were the same as for the static loaded tire model: 90psi, 100psi, and 110psi. It was found that there are some differences between the static results and the free rolling results. First, the normal stress contours of the free rolling tire model are shifted forward. Because of the deformation in the leading portion of the contact patch, the vertical pressures are shifted forward. The centroid of the vertical force does not pass through the spin axis and therefore rolling resistance is generated. Second, the high stress areas are moved toward the two sidewalls in the free rolling tire model. High stress areas are increased in fore-back direction. When the deflection of the rolling tire model is

increased, this phenomenon is more pronounced. Deformations for the rolling tire model were larger in the contact areas due to frictional forces between the tire and the pavement. Sidewall areas carry larger load because they have higher stiffness. So the higher stresses of the free rolling tire model are shifted to the sidewall areas. Third, the contact areas are found to be smaller for the free rolling tire model. For the rolling tire, the inertial force of the rolling tire has an effect on the contact area. When the tire is rolling about its axle, the centrifugal force is distributed in the tire tread. Since the centrifugal force is proportional to ω^2 (ω is the angular velocity of the rolling tire) a higher rotating speed produces a larger centrifugal force. Similar to increasing tire pressure, increasing the centrifugal force will increase the tire stiffness. Thus the contact area will be decreased at a given deflection level. Fourth, the normal maximum stress for the free rolling tire model is higher than that of the static loaded tire at higher tire pressure levels. At a pressure of 90 psi and a deflection of 49.6 mm, the maximum normal stresses are 1.492 Mpa and 1.481 Mpa for the statically loaded tire and the free rolling tire respectively. At a pressure of 100 psi and a deflection of 48.9 mm, the maximum normal stresses are 1.54 Mpa and 1.628 Mpa for the statically loaded tire and the free rolling tire respectively. At a pressure of 110 psi and a deflection of 48.4 mm, the maximum normal stresses are 1.584 Mpa and 1.694 Mpa for the statically loaded tire and the free rolling tire, respectively.

It was mentioned earlier, the static average stresses are used in pavement design. Even for the static loaded tire model, normal stresses are underestimated by the static average. For the free rolling tire at 100 psi and 110 psi the underestimation is worse. When deflections of the static tire were close to 50 mm, the ratio between the maximum normal stresses and the average normal stresses is close 2.0. For a free rolling tire at 100 psi and

110 psi the ratio is 2.045 and 2.12. It seems reasonable to use a multiplying factor of 2.2 to modify the average normal stress for the approximate actual normal stress found for the free rolling model at 100 psi and 110 psi. As discussed earlier, the tire/pavement model is with smooth tread and rigid pavement. In the real world, tires may have different types of grooves and pavements may be concrete or asphalt. The detailed tire/pavement information will change the factor value.

For a pressure level of 100psi, two deflections and two velocities were shown. It can be seen that normal stress, shear stresses, and contact area are increased as the deflections increased. This is similar to the static results. Results of the static loaded model and the free rolling model prove that the deflection is a key factor in contact stresses. The results for 45mph and 65mph show that the normal stress, shear stress, and contact area are increased as the speeds increased, but it seems that the deflection has more effect on stress level than the speed does.

By comparing results of the three pressure levels it can be seen that the normal stress and shear stress were increased as the pressure increased. But the contact areas were decreased as the pressure increased. This is similar to the static results.

de (1994) investigated the interaction between a rolling tire and the pavement by using an experimental method. Some of his results were shown in Figure 5.33 to Figure 5.36. The speed of the experiment is quite low, only 5mph. The tire pressure is 90 psi. Two loading levels were used: 40000 N and 80000 N. For comparison purposes, two free rolling cases of the FEA model were listed: 18871 N and 40000 N at 5 mph and 90 psi tire pressure. In de's experimental results, high normal stresses are located at two sidewall areas. The maximum normal stress is about 0.75 Mpa and 1.5 Mpa for 40000 N and

80000 N, respectively. The maximum normal stress is a little shifted forward. These results are similar to the FEA simulations discussed previously, although de's tire model is not same as the FEA model. Maximum normal stress of the FEA model is 1.42 Mpa for 40000 N vertical load. It is almost twice de's result at 40000 N. Since the tire structures are different, the two results can not be compared directly, but they have similar normal stress distribution and shear distribution profiles. These results do provide a reference for tire/pavement interaction information. Also, since de used pins to measure the normal load, it is possible that the highest local loads were missed. One wonders also if inertial and dynamic effects were properly accounted for in the experimental work, particularly in the choice of strain gages. Unfortunately, de did not provide tire properties in the form of load deflection-curve so direct quantitative comparison can not be pursued.

6.2 Traction or Braking Tire Model

Results for the traction or braking tire model were illustrated in Table 5.5. The same pressure levels as for the static loaded tire model were considered: 90psi, 100psi, and 110psi. Normal stress contours for traction models are shifted forward more than they are for the free rolling model. The reason for the shifting was discussed in the previous section. Since the rolling resistance is larger for a traction model, the normal stress contours are shifted more. For the braking model the normal stress contours are shifted backward. As mentioned earlier, sidewall areas carry larger load. High stresses for traction models are also located toward sidewalls. But high stresses for braking models are located at a small area toward sidewalls.

For traction models and braking models, the contact areas are larger and contact stresses are higher than for the free rolling model. High normal stresses for braking models are located in smaller areas than for traction models, and the maximum normal stress is higher than for the traction model. For the braking model at a pressure of 90 psi and a deflection of 49.6 mm, the maximum normal stress is 2.442 Mpa when the translation speed is 65 mph and the rotating speed is 55 mph. In this case the tire is slipping. These data show that traction and braking are much more critical in terms of stress than is the free rolling model. Braking models are more critical than traction models. For the braking model the ratio between the maximum normal stress and the static average stress is 3.24.

For the traction model at a pressure of 100 psi two deflections were considered. As with the other two models, a higher deflection creates a higher stress and a larger contact area.

By comparing results for the three pressure levels it can be seen that the normal stress and shear stress increased as the pressure increased. For the static loaded models and free rolling models, the contact areas decreased as the pressure increased. But for traction or braking models, the contact areas don't have the same trend. Deformations in contact areas are larger for traction models or braking models. They produce the larger contact areas for traction models or braking models. The effect of tire pressure on the contact area is not as obvious as for the static loaded models and free rolling models. Results show that traction models or braking models are more critical at higher pressure than free rolling models.

In comparison with a free rolling model, the interface shear stresses are quite high. The maximum interface shear stress for the braking model is 1.609 Mpa. The maximum shear stress ratio between the braking model and the free model is 5.4. The maximum shear stress is a very important factor in pavement design.

6.3 Slip-Rolling Tire Model

Results for a slip-rolling tire model were illustrated in Table 5.6. The same pressure levels as for the static loaded tire model were considered: 90psi, 100psi, and 110psi. The high stress areas are moved toward the sidewall in the slip direction. The contact areas are smaller than were found for the free rolling model. The maximum normal stresses are higher than for free rolling models and traction or braking models. For the slip-rolling model at a pressure of 100 psi, 65 mph, and 3-degree slip angle the maximum normal stress is as high as 2.964 Mpa. It is 3.72 times the static average normal stress.

In this analysis the slip angle was increased from zero to three degrees. Results show that a larger slip angle produced higher normal stress and shear stress.

For the slip-rolling model at a pressure of 90 psi, two friction coefficients were considered: 0.9 and 1.0. Results are slightly different between these two cases. When slip angles was increased, stresses difference was increased. For a 3-degree case the maximum normal stresses are 2.546 Mpa and 2.631 Mpa for friction coefficients of 0.9 and 1.0, respectively.

For the slip-rolling model at a pressure of 100 psi, two speeds were considered: 45 mph and 65mph. Results show that the high speed created a little higher stress. The normal stresses at a 3-degree slip are 2.488 Mpa and 2.964 Mpa for speeds of 45 mph and

65 mph respectively. The transverse shear stresses at a 3-degree slip are 0.8206 Mpa and 1.058 Mpa respectively.

For the slip-rolling model at a pressure of 100 psi, two deflections were considered: 29 mm and 49 mm. As for other loading cases, a higher deflection created higher stresses. The normal stresses at a 3-degree slip are 1.74 Mpa and 2.964 Mpa for deflections of 29 mm and 49 mm respectively. The transverse shear stresses at a 3-degree slip are 0.6956 Mpa and 1.058 Mpa respectively.

For the slip-rolling model at a slip angle of 3 degree the normal stresses for 90 psi, 100 psi, and 110 psi are 2.631 Mpa, 2.964 Mpa, and 2.713 Mpa. In previous tire loading models, a higher pressure created a higher normal stress. But for the slip-rolling model, results for 90 psi and 110 psi are quite close. At a pressure of 100 psi the normal stress is the highest one among the three pressure levels. It shows that a little higher pressure than the design pressure helps support normal load.

Chapter 7

CONCLUSIONS

A tire/pavement interaction is simulated using the finite element method for a truck tire rolling over a rigid pavement. In this analysis the tire is modeled by using two-dimensional and three-dimensional elements in which geometric nonlinearities and anisotropic materials are included. Different pressures, loads or deflections, speeds, slip angles, braking or traction, and friction are considered. The analysis successfully provides contact interface stress distributions for a tire rolling over a rigid pavement. The results show that the finite element method is a very useful and powerful tool for tire/pavement interaction analysis.

Results for a statically loaded tire describe the response of the tire to inflation pressure loads, contact loads, and normal static loads against a rigid flat plate. Numerical results of load-deflection curves are quite close to experimental results obtained from the literature. Contact shapes and contact areas differ at different load levels. The maximum normal stress is located at the center of the contact area at lower load; the maximum normal stress is separated into two parts located around the sidewalls at higher load. The ratio between the maximum normal stress and average normal stress is as high as 1.9817 for the tire model with a pressure of 90 psi and 50 mm deflection. The data shows that the

normal stress levels are seriously underestimated if the average normal stress is used in pavement design.

Results for a rolling tire describe the truck tire subjected to inflation pressure loads, normal loads, and contact loads against a rigid pavement under moving conditions including braking, traction, and slip. Results from this investigation lead to the following observations and conclusions:

1. For a free rolling tire model, normal stress contours of the free rolling tire model are shifted forward; high stress areas are moved toward to two sidewalls; high stress areas are increased in fore-back direction; normal maximum stresses at higher tire pressure (100 psi and 110 psi) are higher than for the static loaded tire. At a deflection of 50 mm and a speed of 65 mph, maximum normal stresses for free rolling models are increased by 5.7 % and 6.9 % beyond those for the static loaded model for 100 psi and 110 psi tire pressure respectively.
2. For a free rolling tire model at a deflection of 50 mm and a speed of 65 mph, the ratio between the maximum normal stress and the average static normal stress is above 2.0 for both 100 psi and 110 psi.
3. For a free rolling tire model, increasing deflection, and speed will produce higher contact stress; at higher tire pressure (100psi and 110 psi) increasing tire pressure will produce higher contact stress. Among the three factors, deflection has more effect on contact stresses and contact areas than the other two. For a tire pressure of 100 psi and a speed of 65 mph, the maximum normal stress of the free rolling model is increased by 32.6 % when the deflection is increased from 29 mm to 50 mm. At a deflection of 50 mm and a speed of 65 mph, the maximum normal stress is increased by 9.9%

when the tire pressure is increased from 90 psi to 100 psi. The maximum normal stress is increased 10.7 % when the tire pressure is increased from 90 psi to and 110 psi. For a tire pressure of 100 psi and a deflection of 50 mm, the maximum normal stress is increased by 2.5 % when the speed is increased from 45 mph to 65 mph.

4. Comparisons with de's experimental work suggest that they have similar normal stress distribution and shear distribution profiles. These results do provide a reference for tire/pavement interaction information. Also, since de used pins to measure the normal load, it is possible that the highest local loads were missed. One wonders also if inertial and dynamic effects were properly accounted for in the experimental work, particularly by choice of strain gages. Unfortunately, de did not provide tire properties such as a load deflection-curve, so direct quantitative comparison can not be pursued.
5. For traction or braking tire models, normal stress contours for the traction models are shifted forward more than for the free rolling model; normal stress contours for the braking models are shifted backward.
6. For traction or braking tire models, contact areas are larger and contact stress are higher than for the free rolling model. For a tire pressure of 100 psi, a deflection of 50 mm, and a speed of 65 mph, the maximum normal stress for the traction model is 28.7 % higher than that for the free rolling model; the contact area for the traction model is 4.99 % larger than that for the free rolling model. High normal stresses for the braking models are located in a smaller area than for traction models. The maximum normal stress for the braking model is higher than that for traction. At a tire pressure of 90 psi, a deflection of 50 mm, and a speed of 65 mph, the contact area for the braking model is 2.3 % smaller than that for the traction model; the normal stress

for the braking model is 34.8 % higher for the braking model than that for the traction model.

7. For traction or braking tire models, increasing deflection will produce higher contact stress and larger contact area; increasing pressure will produce higher contact stress. For a tire pressure of 100 psi and traction at 65 mph, the maximum normal stress for the traction model is increased by 25.6 % when the deflection is increased from 29 mm to 50 mm; and the contact area is increased by 49.4 % when the deflection is increased from 29 mm to 50 mm. At a deflection of 50 mm and traction at 65 mph, the maximum stress of the traction model is increased by 4.7 % when the tire pressure is increased from 100 psi to 110psi.
8. The maximum interface shear stress for the braking model is higher than that for static loaded model and free rolling model. At a tire pressure of 90 psi, a deflection of 50 mm, and a speed of 65 mph, the maximum shear stress ratio between the braking model and the free model is 5.4.
9. For the slip-rolling tire model, high stress areas are moved toward the sidewalls in the slip direction. The contact areas are smaller than for the free rolling model. The maximum normal stresses are higher than for free rolling models and traction or braking models. At a pressure of 100 psi, a deflection of 50 mm, and a speed of 65 mph, the contact area for the slip-rolling model with 3^0 slip angle is 9.2 % less than that for the free rolling model. At a tire pressure of 100 psi, a deflection of 50 mm, and a speed of 65 mph, the maximum normal stresses for a slip-rolling model with 3^0 slip angle is 28.3 % and 45.1% higher than that for free rolling model and traction model respectively.

10. For the slip-rolling tire model, a larger slip angle produces higher normal stress and shear stress. For a tire pressure of 110 psi, a deflection of 50 mm, and a speed of 65 mph, the maximum normal stress of the slip-rolling model is increased by 53.5 % when the slip angle is increased form 0.9^0 to 3^0; and the maximum shear stress of the slip-rolling model increased by 132.5 % when the slip angle is increased from 0.9^0 to 3^0.
11. For the slip-rolling tire model, increasing deflection, friction, speed, and slip angle will produce higher contact stress. Among these factors deflection has more effect than the other parameters do. For a tire pressure of 100 psi, a deflection of 50 mm, and a speed of 65 mph with a slip angle of 3^0, the maximum normal stress of the slip-rolling model is increased 70.3 % when the deflection is increased from 22 mm to 50 mm.
12. The maximum ratios of max/av. normal stress vary from 1.98 for static case to 1.97 for the free rolling case, and 3.22 for the traction case to 3.29 for the slip rolling case. These findings suggest that the average stress used in the AASHTO seriously underestimates the maximum stresses served by pavements, with the result that highways can be seriously underdesigned.

Chapter 8

FUTURE WORK AND RECOMMENDATIONS

For both the automotive industry and highway system designers, truck tire/pavement contact analysis, a very complicated procedure, is important. Based on the results obtained in this study, the following recommendations for future research on the analysis of rolling tire/pavement contact are offered:

1. Consider different road profiles. It is known that unsmooth surfaces induce heavier load between pavement and vehicle tire. Investigating a rolling tire over unsmooth pavements will provide very useful data for both pavement design and tire analysis.
2. Consider dynamic loading due to bouncing. It is known that bouncing accelerates masses, which may produce loads as high as several times actual load. This is a very critical loading case, but the analysis is complicated. Experimental bouncing data are needed as input information for tire/pavement interaction analysis.
3. Consider truck tires with typical grooves and less-idealized pavement models. In general, grooves of a tire created higher contact stresses than a smooth tire. There are various types of grooves. It is very useful to analyze tires with typical types of grooves as they roll over asphalt and concrete pavements.

4. Consider temperature influences. The tire/pavement interaction is a thermal-mechanical coupled problem. In real situations, trucks roll over pavements through many seasons with temperatures that vary greatly. Material properties for tire and pavement are temperature-dependent. Investigating the effect of temperature on the tire/pavement contact is important for the automotive industry and for highway system designers. First, temperature-related materials properties and temperature change information related to tires rolling over various kinds of pavements should be obtained by experimental or numerical methods. Second, researchers need to simulate the tire rolling over pavements under varying conditions such as different temperatures and periods of rolling time.
5. More experimental investigation is needed to provide data that will guide computational further efforts.

BIBLIOGRAPHY

AASHTO (1993,) *Guide for Design of Pavement Structures*, The American Association of State Highway and Transportation Officials, Washington, D.C. 2001.

Aliabadi, M. H., and Brebbia, C. A. edited (1993,) *Contact Mechanics, Computational Techniques*, Computational Mechanics Publications, Boston, MA.

Altair Computing, Inc. (1995,) *HyperMesh Documentation*. Altair Computing Inc.,Troy. MI 48084.

Ashton, J.E., Halpin, J.C., and Petie, P.H. (1969,) *Primer on Composite Materials Analysis*, Technomic, Stamford, Conn.

Barbin, W. W. (1994,) "Tire Compound Development," in *Rubber Products Manufacturing Technology* (edited by Bhowmick, Hall, and Benarely), Marcel Dekker, Inc.

Chatti, K. (1992,) *Dynamic Analysis of Jointed Concrete Pavements Subjected to Moving Transient Loads*, Ph. D. Dissertation, The University of California, Transportation Center.

Chen, S.S. (1987,) *The Response of Multi-layered Systems of Dynamic Surface Loads*, Ph. D. Dissertation, The University of California-Berkeley.

Clark, S. K. (edited) (1981,) *Mechanics of Pneumatic Tires*, U.S. Department of Transportation, National Highway Traffic Safety Administration, Washington, DC 20590.

Cook, R. D., Malkus, D. S., and Plesha, M. E. (1989,) *Concepts and Applications of Finite Element Analysis*, John Wiley & Sons, Inc., New York.

de, B. M. (1994,) Measurement of Tyre/Pavement Interface Stresses under Moving Wheel Loads, Report, Center for Structural Mechanics: University of Pretoria, South Africa.

DeEskinazi, J., Yang, T. Y., and Soedel, W. (1978,) "Displacements and Stresses Resulting from Contact of a Steel Belted Radial Tire with a Flat Surface," *Tire Science and Technology*, TSTCA, Vol. 6, No. 1.

Fancher, P. S., et al. (1986,) *Factbook of The Mechanical Properties of The Components For Single-Unit and Articulated Heavy Trucks*, DOT-HS-807125, University of Michigan, Transportation Research Institute, Ann Arbor, MI.

Faria, L. O., Bass, J. M., Oden, J. T., and Becker, E. B. (1989,) "A Three-Dimensional Rolling Contact Model for a Reinforced Rubber Tire," *Tire Science and Technology*, TSTCA, Vol. 17, No. 3.

Faria, L. O., Oden, J. T., Yavari, B., Tworzydlo, W. W., Bass, J. M., and Becker E. B. (1992), "Tire Modeling by Finite Element," *Tire Science and Technology*, TSTCA, Vol. 20, No. 1.

Federal Highway Administration (1995,) *Pavement Primary Response Testing*, Federal Highway Administration, McLean, VA 22101.

Fleming, R. A. and Livingston, D. I. (edited) (1979,) *Tire Reinforcement and Tire Performance*, ASTM STP 694, American Society for Testing and Materials.

Ford, T. F. and Charles, R. S. (1988,) *Heavy Duty Truck Tire Engineering*, Society of Automotive Engineers, Inc., Warrendale, PA 15096.

Gillespie T. D. (1985,) *Heavy Truck Ride*, SP-607, SAE the Engineering Resource for Advancing Mobility, The Thirty-First L. Ray Buckendale Lecture, Society of Automotive Engineers, Inc.

Gillespie T. D. (1992,) *Fundamentals of Vehicle Dynamics*, Society of Automotive Engineers, Warrendale, PA.

Hendrick, J. K., Marlow, M. J., and Brademeyer, B. (1992,) The Simulation of Vehicle Dynamic Effects on Road Pavements, Report, FHWA-RD-90-108, U.S. Department of Transportation, Federal Highway Administration, November.

Hibbit, Karlsson & Sorensen, INC. (1998,) *Abaqus Theory Manual* Hibbit, Karlsson & Sorensen, INC., Pawtucket, RI 02860-4847.

Hibbit, Karlsson & Sorensen, INC. (1998,) *Abaqus/Standard User's Manuel*, Hibbit, Karlsson & Sorensen, INC., Pawtucket, RI 02860-4847.

Huang, Y. H. (1993,) *Pavement Analysis and Design*, Prentice Hall, Englewood Cliffs, New Jersey 07632.

Johnson, K. L. (1985,) *Contact Mechanics*, Cambridge University Press, New York.

Kenny, T. M. (1983,) "Prediction of Contained Air Temperature from SAE Standard Rolling Resistance Test Data," SAE Technical Paper Series, 831796.

Kovac, F. J. (1978,) *Tire Technology*, The Goodyear Tire & Rubber Company, Fifth Edition, Akron, Ohio.

Kulakowski B. T. (edited) (1994,) *Vehicle-Road Interaction*, ASTM STP 1225, ASTM Publication Code Number 04-012250-08, American Society for Testing and Materials.

Kuo, C. M., Hall, K. T. and Darter, M. I. (1995,) "A Three -Dimensional Finite Element Model for Analysis of Concrete Pavement Support," The Transportation Research Board 75th Annual Meeting, Washington, D.C.

Mase, G. E., and Mase G. T. (1993,) *Continuum Mechanics for Engineers*, CRC Press, Inc.

Michelin Tire Corporation, *Michelin Truck Industrial & Off The Road Tire Data Book*, Michelin Tire Corporation,

Moore, D. F. (1975,) *The Friction of Pneumatic Tyres*, Elsevier Scientific Publishing Company, Amsterdam, New York.

Mousseau, C. W. and Clark, S. K. (1994,) "An Analytical and Experimental Study of a Tire Rolling Over a Stepped Obstacle at Low Velocity," *Tire Science and Technology*, TSTCA, Vol. 22, No. 3.

Oden, J. T., Lin , T. L., and Bass, J. M. (1988), "A Finite Element Analysis of the General Rolling Contact Problem for a Viscoelastic Rubber Cylinder," *Tire Science and Technology*, TSTCA, Vol. 16, No. 1.

Parhizgar, S., Weissman, E. M., and Chen, (1988), "Determination of Stiffness Properties of Single-Ply Cord-Rubber Composites," *Tire Science and Technology*, TSTCA, Vol. 16, No. 2.

Pottinger, M. G. (1992,) "The Three-Dimensional Contact Patch Stress Field of Solid and Pneumatic Tires," *Tire Science and Technology*, TSTCA, Vol. 20, No. 1.

Pottinger, M. G. and Yager, T. J. (edited) (1986,) *The Tire Pavement Interface*, ASTM Special Technical Publication 929, ASTM Publication Code Number 04-929000-27, American Society for Testing and Materials.

Purdy, J. F. (1963,) *Mathematics Underlying the Design of Pneumatic Tires*, Edwards Brothers Inc., Ann Arbor, Michigan.

Raous, M., Jean, M., and Moreau, J. J. edited (1995,) *Contact Mechanics*, Plenum Press, New York.

Ridha, R. A. and Curtiss, Walter W. (1994,) "Development in Tire Technology," in *Rubber Products Manufacturing Technology* (edited Bhowmick, A. K. et al), Marcel Dekker, Inc.

Ridha, R. A., Satyamurthy, K., Hirschfelt, L. R., and Holle, R. E. (1985a,) "Contact Loading of a Rubber Disk," *Tire Science and Technology*, TSTCA, Vol.13, No. 1.

Ridha, R. A., Satyamurthy, K., Hirschfelt, L. R., and Holle, R. E. (1985b,) "Finite Element Modeling of a Homogeneous Pneumatic Tire Subjected to Footprint Loadings," *Tire Science and Technology*, TSTCA, Vol.13, No. 2.

Roberts, F. L., Tielking, J. T., Middleton, D., Lytton, R. L. and Tseng, K. (1985,) *The Effects of Tire Pressures on Flexible Pavement*, U.S. Department of Transportation Federal Highway Administration, Report, FHWA-TX-85-3721.

Sebaaly, Peter E. (1992,) "Summary of Tire Testing Data," Pavement/Materials Program, Department of Civil Engineering, University of Nevada, Reno, Nevada 89557.

Structural Dynamics Research Corporation (1993,) *I-DEAS FEM User's Guide*, Structural Dynamics Research Corporation.

Tanner, J. A. (1996,) Computational Methods for Frictional Contact with Applications to the Space Shuttle Orbiter Nose-Gear Tire, NASA Technical Paper 3573.

Tinko, M. J. (1984,) "Ply and Rubber Stresses and Contact Forces for Loaded Radial Tire," *Tire Science and Technology*, TSTCA, Vol. 11, No. 1-4, January-December, pp. 20-38.

The Tire and Rim Association, Inc., 1993, *The Tire and Rim Handbook.*

Tseng, N. T. (1987,) "Finite Element Analysis of Freely Rotating Tires," *Tire Science and Technology*, TSTCA, Vol. 15, No. 2, April-June, pp. 134-158.

White, T. D., Zaghloul, S. M., Anderton, G. L., and Smith D. M. (1995,) "Use of a Three-Dimensional, Dynamic Finite Element Model to Study the Effect of Unbound Layer Characteristics on Pavement Response to a Moving Aircraft Load," Transportation Research Board, 74th Annual Meeting, January 22-28, 1995, Washington, D.C.

Zienkiewicz, O. C., and Taylor, R. L. (1989,) *The Finite Element Method*, McGraw-Hill Book Company., New York.